Special Cardiology Edition

MAGNETOM Flash

The Magazine of MRI

siemens-healthineers.us/magnetom-world

SIEMENS Healthineers

In this combined Cardiac/Angiography edition of the MAGNETOM Flash magazine, we showcase several game-changing tools available in the United States that are making a positive impact on patient care, in particular those suffering from cardiac and peripheral vascular disease. Starting with Cardiac MR, this modality can provide accurate assessment of the heart's structure, function, and viability. In the past, patients who would benefit from this exam, such as those with difficulty holding their breath or arrhythmias, often were excluded. With new applications like Compressed Sensing Cardiac Cine coming to market, we are expanding the patient population that can undergo a cardiac MR exam. In addition, MR Angiography with contrast typically is contra-indicated in patients suffering from both peripheral vascular disease and renal insufficiency, excluding these patients from a diagnostic exam. With new, non-contrast techniques, we are able to image these patients and help confirm their diagnoses. Finally, our Dot engines have reduced the complexity of both Cardiac and Angiography exams, ultimately removing variability from the scanning process and improving workflow efficiency.

Editorial Board

We appreciate your comments.
Please contact us at magnetomworld.med@siemens-healthineers.com

Antje Hellwich
Editor-in-chief

Reto Merges
Head of Scientific Marketing

Sunil Kumar S.L., Ph.D.
Senior Manager Applications, Canada

Wellesley Were
MR Business Development Manager Australia and New Zealand

Gary R. McNeal, MS (BME)
Advanced Application Specialist, Cardiovascular MR Imaging Hoffman Estates, IL, USA

Review Board

Daniel Fischer
Head of Outbound Marketing MR Applications

Christian Geppert, Ph.D.
Head of Cardiovascular Applications

Efren Ojeda
MR Marketing Applications Center

Michaela Schmidt
Cardiovascular Application Development

Christian Schuster, Ph.D.
Product Manager Cardiovascular

Gaia Banks, Ph.D.
Global Segment Manager Cardiovascular MR

Additional Resources

Webinars: Industry experts discuss the latest trends and innovations in MRI.
siemens-healthineers.us/mr-webinars

Case Studies: Customers share how our MRI solutions support their success.
siemens-healthineers.us/mr-casestudies

Contents

Cardiac

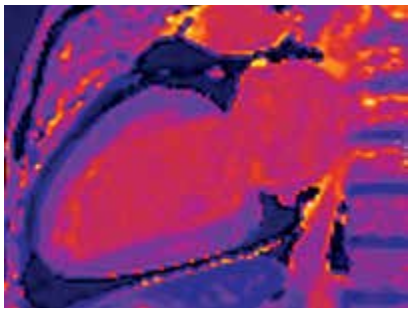

CS Cardiac Cine

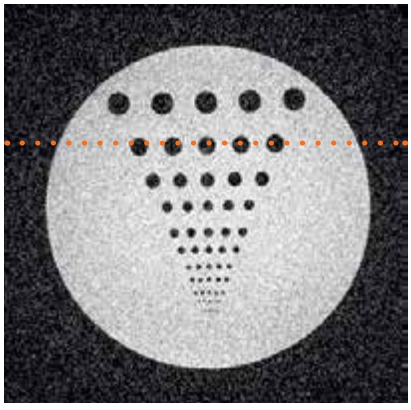

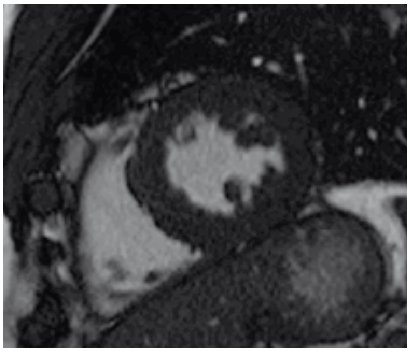

Angiography

QISS

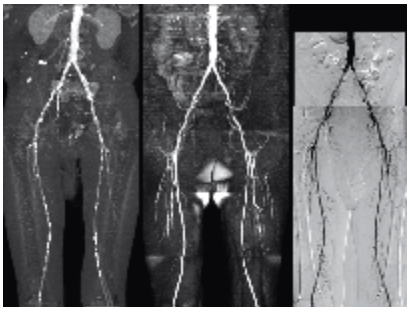

Thoracic

Case Report: Acute Myocardial Syndrome in a 37-Year-Old Patient with Severe Renal Impairment

S. A. Mohiddin; A. S. Herrey
Institute of Cardiovascular Science, University College London;
The Inherited Cardiovascular Diseases Unit and Cardiac Imaging Department,
The Barts Heart Centre, London, UK

A 37-year-old lady was admitted to our institution with chest pain and pain in her left arm, but no shortness of breath. Preceding the admission she had experienced symptoms of an acute upper respiratory tract infection.

Her past medical history included hypertension, hypothyroidism, hyperprolactinaemia, focal sclerosing glomerulosclerosis with stage IV chronic kidney disease, eGFR 17 ml/min, treated tuberculosis and three first trimester miscarriages.

On admission, her hs- troponin T was > 7,000 ng/L (normal < 30 ng/L). Her ECG was largely unchanged from a previous one taken in 2013 meeting LVH criteria, but otherwise unremarkable.

Her echocardiogram showed low-normal left ventricular systolic function with akinesis of the mid inferior and mid infero-septal segments with an estimated EF of 55%.

On coronary angiography, her coronary arteries were unobstructed.

To confirm the working diagnosis of myocarditis, she underwent Cardiovascular Magnetic Resonance (CMR) imaging on our MAGNETOM Aera 1.5T (Siemens Healthineers, Erlangen, Germany). In view of her severe renal impairment, no gadolinium contrast was given.

This was reported as showing normal biventricular size, mild systolic impairment with hypokinesis of the antero-septum, infero-septum and inferior wall. Non-contrast tissue characterisation with T1 and T2 mapping identified markedly increased T1 and T2 values matching (and extending beyond) the regional wall motion abnormalities, confirming the diagnosis of florid acute myocarditis.

Subsequently, her troponin levels were falling and she was discharged pain free a few days later.

A month later, her EF on echo had normalised with mild residual inferior hypokinesis and her troponin was normal at 18 n/L. Her repeat CMR, however, showed persistent myocardial inflammation, but with falling T2 values.

In summary, non-contrast myocardial mapping in this case was used to establish and confirm a diagnosis of myocarditis and also to monitor progress.

Contacts
Anne S. Herrey
anna.john@doctors.org.uk

Panel 1

The T1 maps (MOLLI) show extensive interstitial expansion in the septum and the inferior wall on the first scan. On the second (F_UP) scan, there is incomplete resolution in the inferior wall and limited change in the septum.

a) On the two-chamber view (T1_MOLLI_2cha and F_UP_T1_MOLLI_2cha) there is increased signal in the inferior wall.

b) In a four-chamber orientation (T1_MOLLI-4cha and F_UP_T1_MOLLI_4cha), there is increased signal in the septum.

c) In the short axis views (T1_MOLLI_mid-SAX and F_UP_T1_MOLLI_mid_SAX), both increased signal can be seen in the septum and the inferior wall.

Panel 2

The matching T2 maps confirm myocardial oedema matching the areas of high native T1 values. The florid changes seen in the initial scan are less impressive at follow-up (F_UP), but still present.

a) High T2 signal is seen in the two-chamber view in the inferior wall (T2-4cha and F_UP_T2_4cha).

b) In the four-chamber orientation, there is increased signal in the mid septum.

c) The short axis view confirms similar changes in septum and inferior wall compared to the T1 maps.

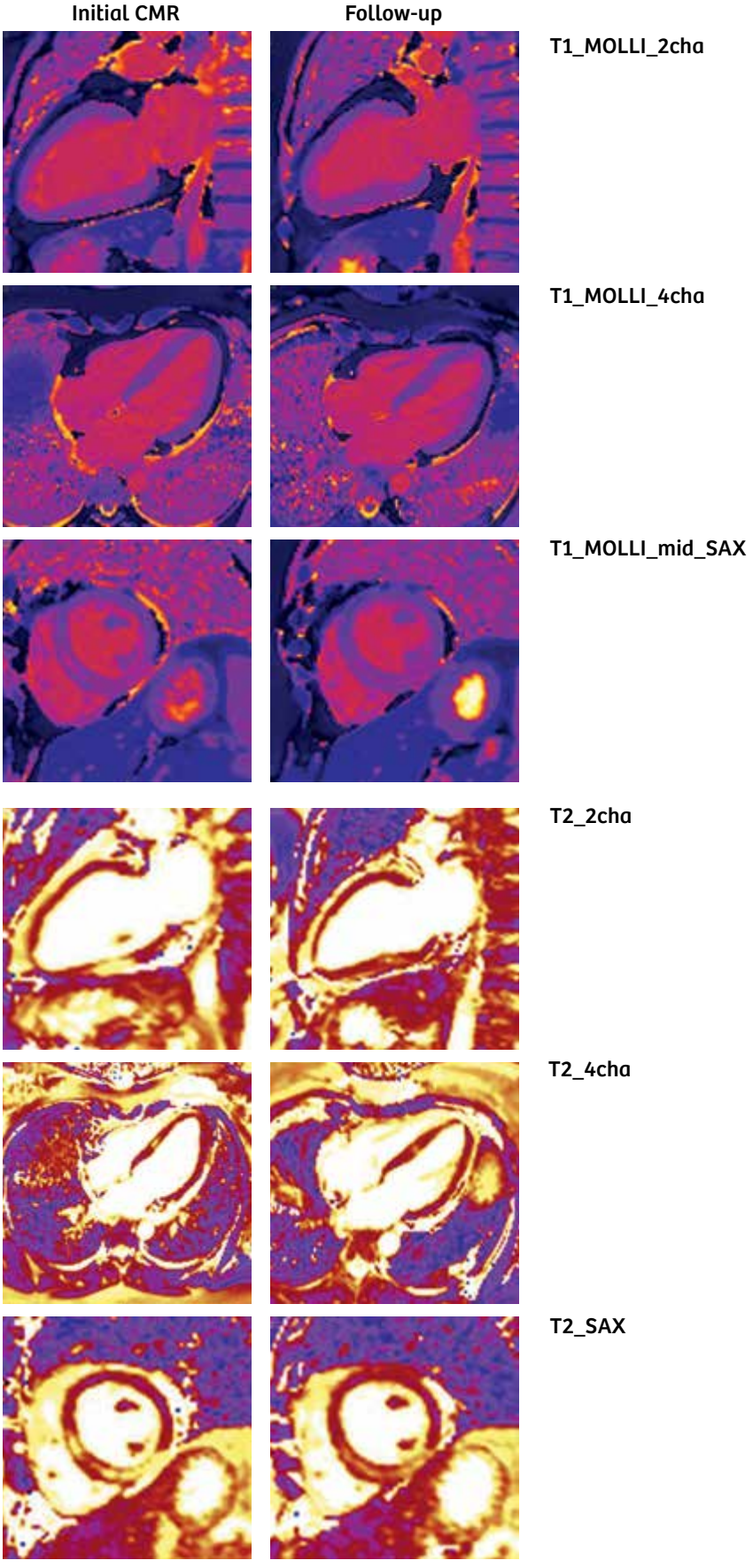

syngo.MR Cardiac 4D Ventricular Function

Bernd J. Wintersperger, M.D. EBCR FAHA[1]; Arne Littmann, Ph.D.[2]
[1]Department of Medical Imaging, University Health Network, University of Toronto, Canada
[2]Siemens Healthineers, Erlangen, Germany

Objectives and definitions

Cardiac MRI background
In developed countries, approximately 2% of adults present with heart failure and in the elderly population (> 65), this increases to 6–10%. [1, 2]

Cardiac MRI is considered as the gold standard with respect to accuracy and reproducibility of volumes, mass, and wall motion. [3]

Cardiac MRI primarily aims to assess cardiac morphology and functional parameters such as ventricular volumes, ejection fraction, mass and regional wall motion. Furthermore, cardiac MRI provides an even more detailed evaluation of the myocardial tissue including the evaluation of ischemia, myocardial viability and scar, as well as potential edematous changes which may be important aspects towards therapy guidance. In a large variety of cardiac diseases, patient prognosis is closely related to the left ventricular ejection fraction (LVEF), with a low ejection fraction being related to higher morbidity and mortality.

By definition, the ventricular ejection fraction (EF) is the percentage of blood that is being 'ejected' from the maximally filled ventricle during systole of each heartbeat (Fig. 1). Mathematically, cardiac volumes and ejection fraction are related by the following equation:

$$EF = \frac{EDV - ESV}{EDV} \times 100$$

Where:

- EDV (End-diastolic volume) relates to the maximum volume of the ventricle at the end of the filling phase of the cardiac cycle (diastole) with all valves closed just prior to the ventricular ejection.
- ESV (End-systolic volume) relates to the minimum volume of the ventricle at the end of the ejection period (systole) with all valves closed just before ventricular filling.

Measuring volumes

To calculate LVEF, the volume of the ventricular cavity needs to be assessed at two different specific time points within the cardiac cycle, at end-diastole and at end-systole.

In order to do so, imaging data is acquired using cine techniques (typically SSFP techniques) in a series of multiple parallel short axis slices with additional long axis orientations, sampling the entire left ventricle as illustrated in Figure 2.

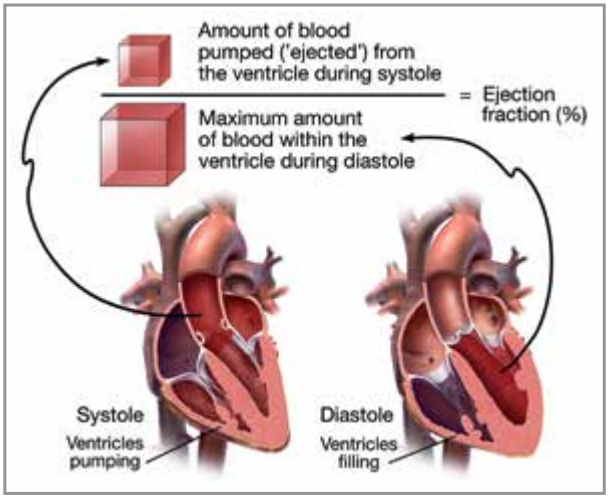

1 Schematic explanation of left ventricular (LV) ejection fraction (EF). Reprodcued with permission from medmovie.com.

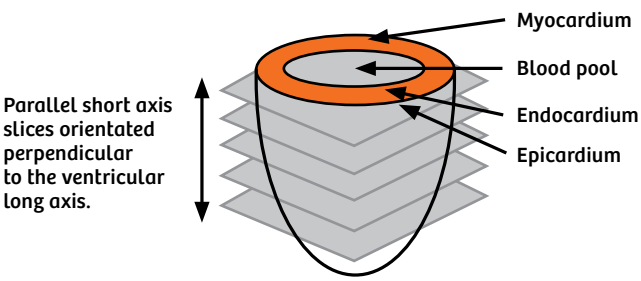

2 Stack of short axis slices sampling the left ventricle.

On a broad outline, during post-processing, contouring of the endocardial border on every single short axis slice allows computing the slice area contained within the endocardial contours. By incorporating the knowledge about the slice extension along the ventricular long axis, the volume represented by this contour at a specific phase can be calculated. The sum of all volumes/slices at end diastole and end systole then results in EDV and ESV, respectively.

Besides these basic operations an important additional aspect needs to be considered: the physiologic shortening and elongation of the ventricle along its long axis over the cardiac cycle.

Through plane motion and base representation

General illustration

During myocardial contraction and relaxation throughout the cardiac cycle, the entire heart demonstrates significant deformation and motion, including translation, rigid body rotation, regional twist, and most importantly a change in long axis dimension.

This change in the long axis dimension is characterized by a ventricular shortening with a physiologic excursion of the basal plane towards the apex during systole (basal descent) while the apex remains relatively stationary (Fig. 3). This through plane motion has been well documented and averages to a max. systolic excursion of ~13 mm in healthy subjects while it is known to generally be reduced in disease [4].

Related to the fact that the LV cross sectional area is at its largest at the base of the heart, the potential error related to through plane motion is generally significant. This may lead to possible inclusion of atrial volume into the LV volume calculation and thus potentially resulting in an overestimation of the LV volume in systole (ESV) with subsequent underestimation of EF [5].

Spatial orientation and position of base plane

The accuracy of the estimated volume of an object is substantially dependent on the way this specific object is spatially sampled by the input images.

In cardiac MRI, the ventricles are typically sampled by a set of parallel short axis 2D slices, where the slice distance and the slice thickness are relatively large in comparison to the in-plane resolution. If all slices are acquired parallel to each other, it is difficult to accurately capture through plane motion with such a

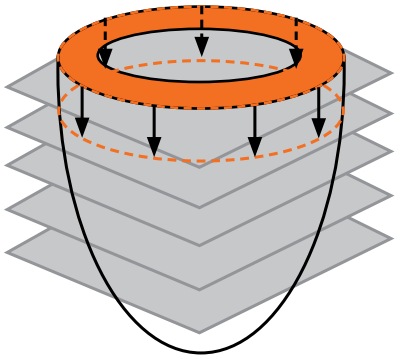

3 Simple illustration of the through plane motion based on a stack of short axis slices.

4

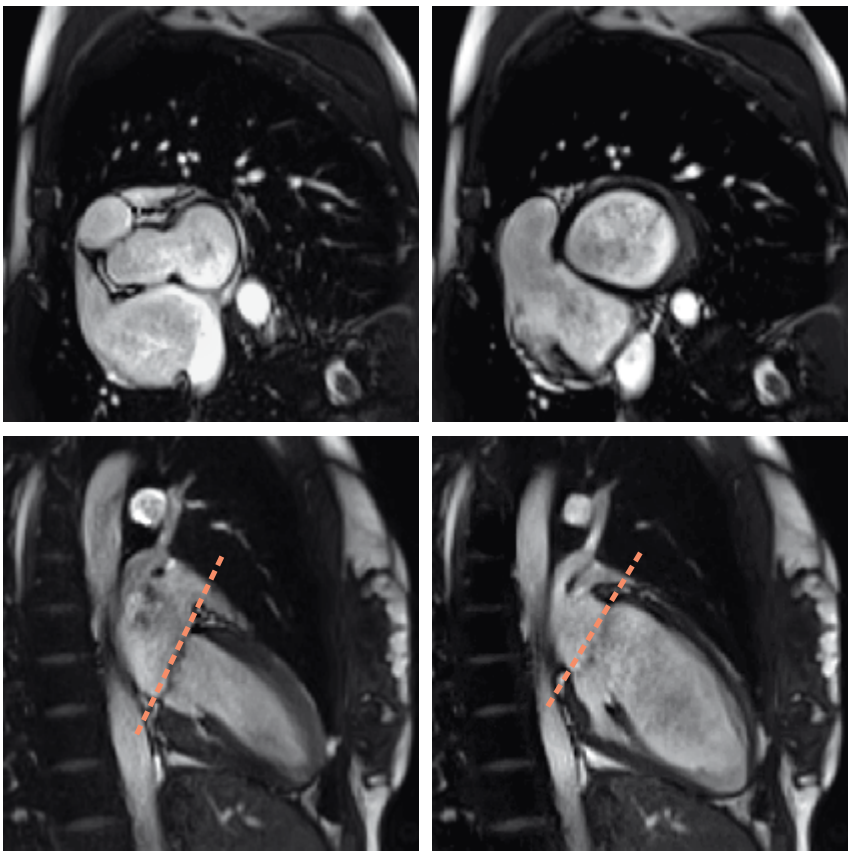

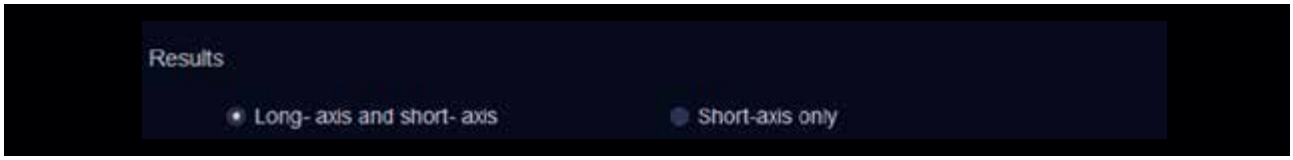

5 Finding Details Dialog in *syngo*.via allows to choose the requested method.

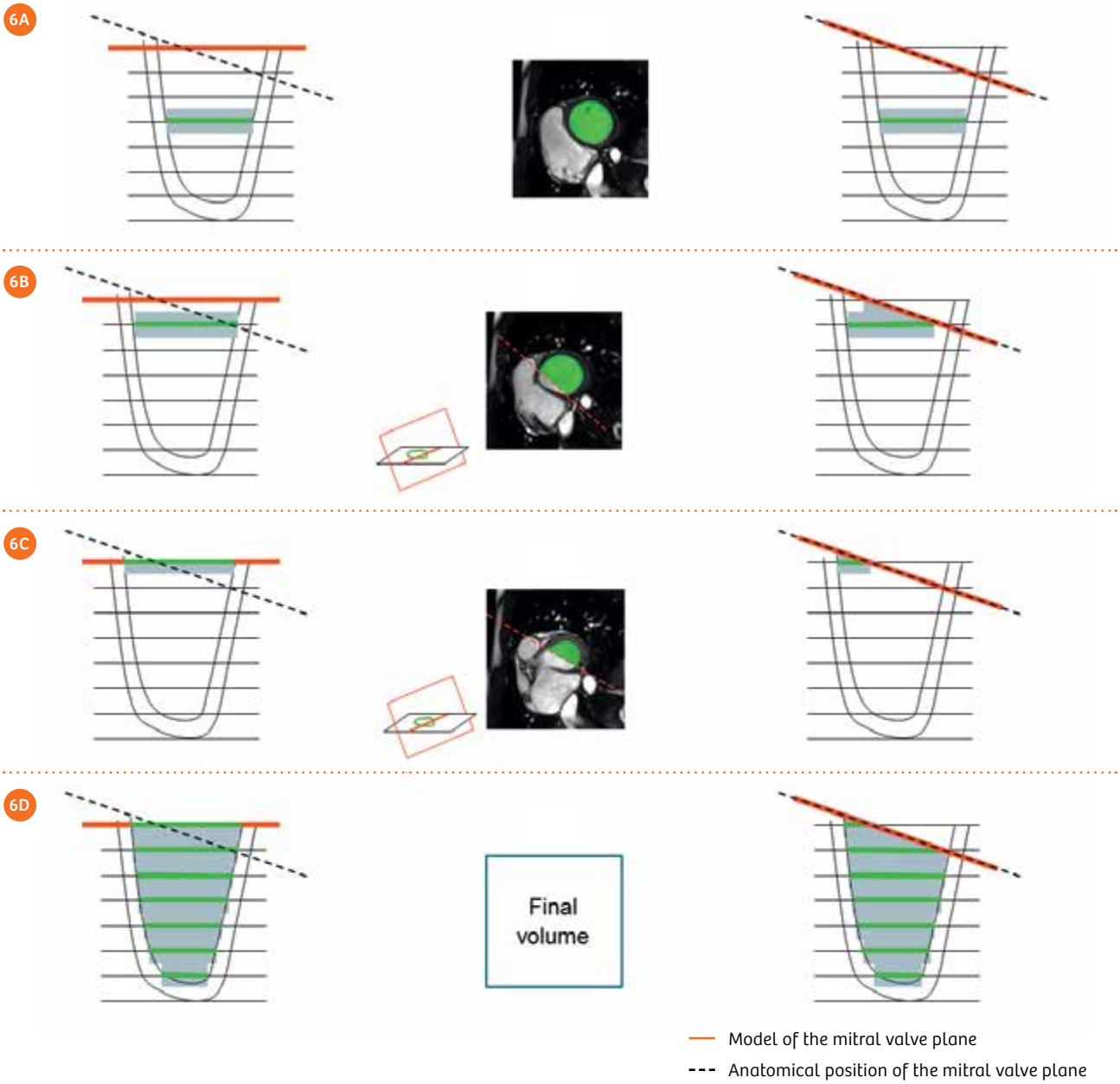

6 Comparison of two possible approaches and the corresponding final volumes (left: short axis only, right: long axis and short axis). The principle is described on a mid-ventricular slice (6A), a basal slice intersecting with the mitral valve plane (6B) and the most basal slice (6C). The representation of the final volume is shown in (6D). When the mitral valve plane intersects the contours, only the portion on the ventricular side of the valvular plane is considered for volumetric calculations until the contours fully reach the mitral valve plane.

sampling pattern. This is especially true if the upper and/or lower boundary of the object of interest may not be entirely parallel to the slice orientation.

Taking a closer look at Figure 4, it becomes obvious that both these conditions are often true for the delineation of the atrio-ventricular (AV) valve (mitral valve in case of the left ventricle) plane: Neither remains it parallel to the short axis over the entire cardiac cycle, nor is the complex through plane motion entirely parallel to the short axis slice orientation (which is represented by the dashed yellow line in the two chamber view).

As illustrated in Figure 4, the exact position of the mitral valve plane and its change over the cardiac cycle are best captured on long axis slices such as the two-chamber view.

Traditional approach to determine LV volume in cardiac MRI

Traditionally, LV volumes in cardiac MRI were determined solely based on a stack of short axis slices. As illustrated in the previous paragraph, the mitral valve and its motion towards the ventricular apex from ED to ES is not adequately visualized in the short axis slices. Consequently, this approach requires special care with regard to inclusion of basal slices in order not to include atrial volume in the LV volumetric evaluation.

In an attempt to at least consistently overcome the short-coming of this "short axis only approach", it is a generally accepted convention to only include basal slices into the LV volumetric evaluation if at least 50% (180 degree) of the LV blood volume is surrounded by ventricular myocardium.

Argus VF Analysis represents an approach for this traditional way to determine ventricular volume which has been in use for decades.

syngo.MR Cardiac 4D Ventricular Function

syngo.MR Cardiac 4D Ventricular Function provides two approaches to compute LV volumes and LV function:

1. "Short axis only" approach: Only short axis slices are used (Argus-like)

- The position of the mitral valve plane in ED and ES is defined by the position of the blood pool point in ED and ES.
- The orientation of the mitral valve plane is by definition parallel to the short axis slices.

2. "Long axis and short axis" approach: Both short axis and long axis are taken into consideration

- The position of the mitral valve plane in ED and ES is defined on the long axis slice(s) by setting "valve points" in ED and ES.
- The orientation of the mitral valve plane is matching the anatomical orientation (which may be not parallel to the short axis slice orientation).

The user can switch between both variants by selecting the desired option in the Finding Details Dialog (Fig. 5).

Both approaches are schematically illustrated in Figure 6.

Conclusion

The described differences in the methodical approach clearly result in variations of quantitative results. Affection of both phases, EDV and ESV, may not necessarily result in a relevant difference in LVEF when compared to the "short axis only" approach. As the orientation of the mitral valve plane and its change over the cardiac cycle is patient specific, there is no simple relationship of both approaches to each other and therefore it is not possible to mathematically convert the volumes computed with the two described approaches.

As illustrated, the "Long-axis and short-axis" approach allows to accurately model any orientation of the mitral valve plane seen on the acquired long axis slices. Since it also allows defining the mitral valve plane independently in ED and in ES, this approach enables the user to also accurately model the apically directed motion of the mitral valve plane from ED to ES. Due to this advantage over the traditional "Short-axis only" approach, the "Long-axis and short-axis" approach is selected as default in *syngo*.MR Cardiac 4D Ventricular Function. It has however to be kept in mind that such an approach requires an adequate cross-reference of short axis and long axis slices in a patients data set and as such consistent breath-holding levels.

References

[1]McMurray JJ, Pfeffer MA (2005). "Heart failure". Lancet 365 (9474): 1877–89.

[2]Dickstein K;Eur. Heart J. 29 (19): 2388–442.

[3]McMurray-EurJHeartFail-14-803.

[4]Walter et al; Circulation 1991; 84:721-731.

[5]Berkovic et al.; European Journal of Radiology 73 (2010) 260–265.

Contact
Bernd J. Wintersperger, M.D. EBCR FAHA
Bernd.Wintersperger@uhn.ca

How-I-do-it: Imaging Proximal Coronary Arteries/ Coronary Root Imaging

Jonathan Richer
Clinical Applications Specialist MRI, Siemens Healthineers, Wayville, SA, Australia

Introduction

Cardiac imaging can be a challenging examination and imaging coronary arteries can be slightly more complex still. There are quite a few protocols available for imaging of these small arteries within the Siemens Healthineers library, such as a breath-hold slab, or using dual gating (respiratory and ECG gating) covering the entire heart or on a targeted approach 3D. Both methods can achieve excellent results. However, they are very patient-dependent, can be time consuming and, in the case of the breath-hold 3D, results are variable due to the very long breath-hold times.

To answer the clinical questions with MRI, the majority of clinicians will typically only need to consider imaging the coronary root in cases of anomalous vessels, and rarely do we need to image the entire vasculature.

Technique

I have modified a 2D TrueFISP sequence in order to image the proximal coronary arteries with a segmented bright blood approach imaging quickly and within a few breath-holds. This can be adapted for both 1.5 and 3T, and protocol parameters are very similar.

You can start by using the TrueFISP sequence in the Siemens Healthineers library.

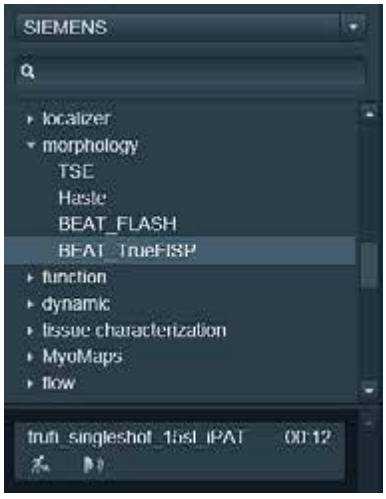

1 Heart → Morphology → BEAT_TrueFISP → **"trufi_singleshot_15sl_iPAT"**

To achieve a nice thin slice thickness in order to minimize partial voluming effects, we need to image at a minimum slice thickness of 3 mm which this sequence won't allow you to do unless we change the RF excitation pulse type from Fast → to Normal. This will disable the VERSE pulse mode and enables standard RF wave form for a better slice excitation profile, thus allowing for a thinner imaging slice.

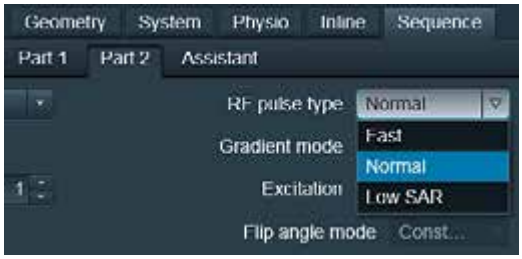

2 Sequence → Part 2 → RF Pulse type → **"Normal"**

Whilst a 3 mm slice thickness is great, we want to eliminate the slice gap, and what this sequence will allow us to do is to set a slice overlap which again helps with minimizing slice partial voluming. This can be set to **-50%** of the slice thickness where we end up with a slice thickness of 3 mm with a 1.5 mm overlap—achieving the similar results to truly acquiring the data at 1.5 mm slice thickness which is outside the possibility of this sequence. We will also need to increase the slice coverage from 25 slices to 30 or 35 slices – ensuring the coronary sinus is covered.

3 Eliminate the slice gap.

Another important parameter to look at is the echo spacing and ideally we must keep this below 3.4 msec. This is particularly important at 3T where an echo spacing of 3.4 or lower will result in less dephasing artifacts. Changing the asymmetric echo from Weak → to Strong and increasing the bandwidth will enable you to reach this target echo spacing.

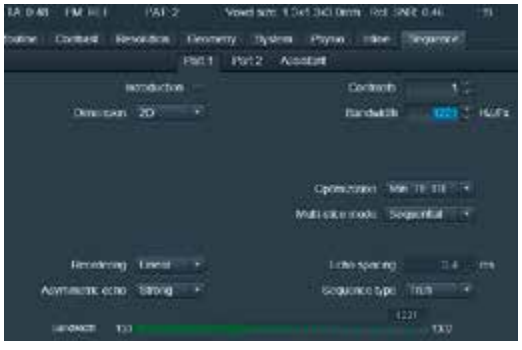

4 Sequence → Part 1 → Asymmetric echo → **"Strong"**

The next step is to ensure appropriate triggering in order to achieving motion-free images. This is done by segmentation where we need to segment/limit *k*-space data acquisitions to appropriate intervals within the cardiac cycle.

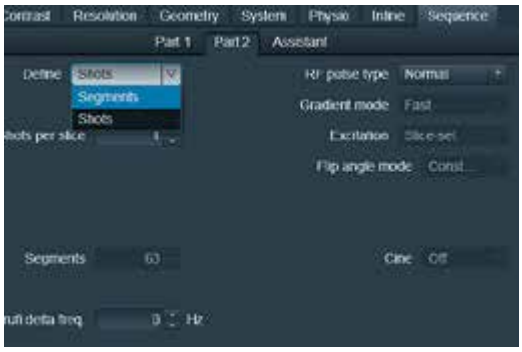

5 Sequence → Part 2 → Define → **"Segments"**

Now we need to increase the segments lines (*k*-space lines acquired in each heart beat) to roughly 30 which gives us a data readout of roughly 100 ms—suitable for most heart rates. To ensure optimal image quality, we must acquire data within the cardiac cycle when the coronary arteries are stationary. This can be done easily with the timing method—by looking at the trigger time on a 4-chamber cine image Trigger Time (TT stamp). Typically the most stable part of the cardiac cycle is in the diastolic phase; however, in fast heart rates, this may be in the systolic phase. Carefully page through the cine images, keep an eye on the right coronary sinus and take note of the trigger time when the heart stops moving in the diastolic phase and when it starts to move again at the end of the cardiac cycle—this will give us the window of opportunity to acquire data.

6A

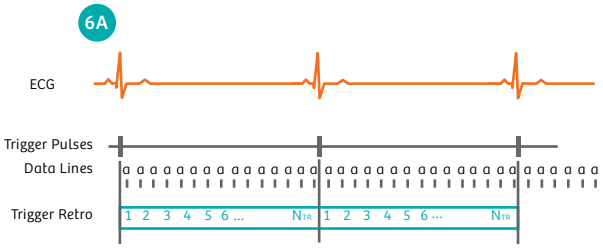

6B

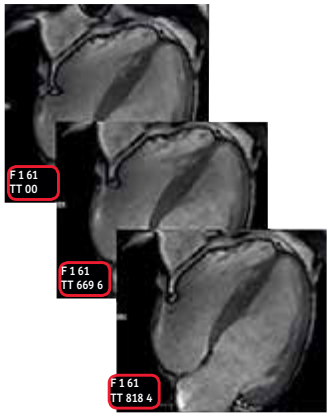

Figure 6A: Trigger Time corresponds to the time within the averaged heart beat in msec.

Figure 6B: Example: Heart stops moving in diastolic phase at "TT**669**" and starts moving again at "TT**818**" (818 - 669 = **149** msec **window**) thus we must **start acquiring after 669** msec and **finish by 818** msec.

Tip: If the heart rate has changed from the start of the examination to the point where we need to do this timing method, the timing will not reflect the patient's current heart rate and therefore you will need to re-run your 4-chamber cine view for accurate results.

In the example above (Figs. 6A, B), we need to start acquiring after 669 msec and finish by 818 msec, and here (Fig. 7) we start at 695 msec and finish at 797 msec (102 + 695 = 797) which is excellent. If we need to start later or earlier, this is done by modifying the Trigger delay. In the case where the heart is not stationary for 102 msec (fast heart rates), we need to decrease the segments (*k*-space lines acquired in each heart beat) to reduce the Data window duration (data readout) fitting for the HR.

7 Hovering on the Trigger delay will display detailed acquisition information: **Data window duration:** how long we acquire data for (data readout) adjusted by segments (increase segments increase window duration and vis versa) **Data window start:** time we start acquiring data which is manipulated by adjusting the Trigger Delay value. Adding the **Data window start** & **Data window duration** gives us the time we finish acquiring.

Now that we've taken care of the triggering and imaging slab, we must ensure we can acquire data within appropriate breath-hold times. This is done by applying breath-hold option under the Physio and PACE card which will then enable you to modify the concatenations (breath-holds). Once you have updated the concatenations, hover over the acquisition time "TA" to see the actual breath-hold times for each concatenation if appropriate for your patient.

8 Physio → PACE → Resp. Control → **Breath-hold** Physio → PACE → Concatenations → **5**

Table 1: Imaging parameters

Parameter name	Value	Parameter change
Slice thickness	3 mm	RF Pulse Type: Normal
Slice gap	-50%	Routine Tab
Segments	30 or appropriate for HR	Sequence Part 2 → define by segments
Breath-hold timing	15 seconds or appropriate	PACE → Breath-hold → Concatenations → 5
Echo spacing	3.4 or less	Sequence → Part 1 → asymmetric echo → Strong & possible BW increase
Flip angle	80–90 (the higher the brighter the blood)	Contrast → Flip angle

Results

This modified sequence will enable you to image the coronary root with a standard 2D bright blood approach within a few breath-holds tailored for your patient's breath-hold capability and heart rate which is generally acquired faster and with higher success rates when compared to the 3D options. Since we are imaging at 3 mm with a 1.5 mm slice overlap, this data will also enable you to create some modified multiplanar reconstructions (MPR) for better visualization in the 3D card. Figures 9 and 10 are some recent examples.

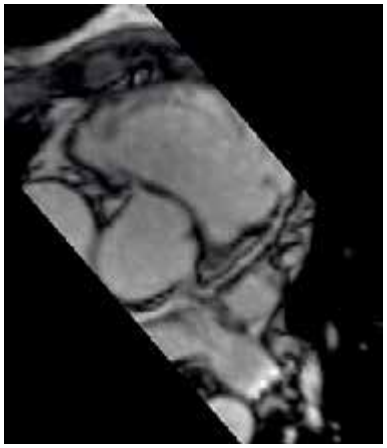

10 34-year-old patient. *(3T MAGNETOM Prisma. Courtesy of Hunter Medical Research Institute, Newcastle, NSW, Australia)*

Conclusion

This technique is a great way to image the proximal coronary arteries using conventional imaging technique standard on any MAGNETOM system. However this technique does have its limitations shared by all normal cardiac imaging, such as consistent heart rates and reproducible breath-holds.

Contact
Jonathan Richer
jonathan.richer@siemens-healthineers.com

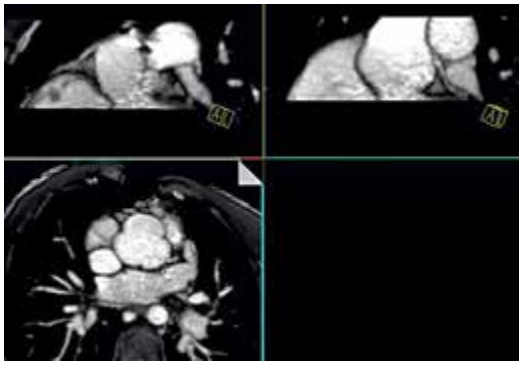

9 7-year-old patient. *(1.5T MAGNETOM Aera. Courtesy of Lady Cilento Children's Hospital, Brisbane, Queensland, Australia)*

Compressed Sensing—the Flowchart

Mathias Blasche; Christoph Forman
Siemens Healthineers, Erlangen, Germany

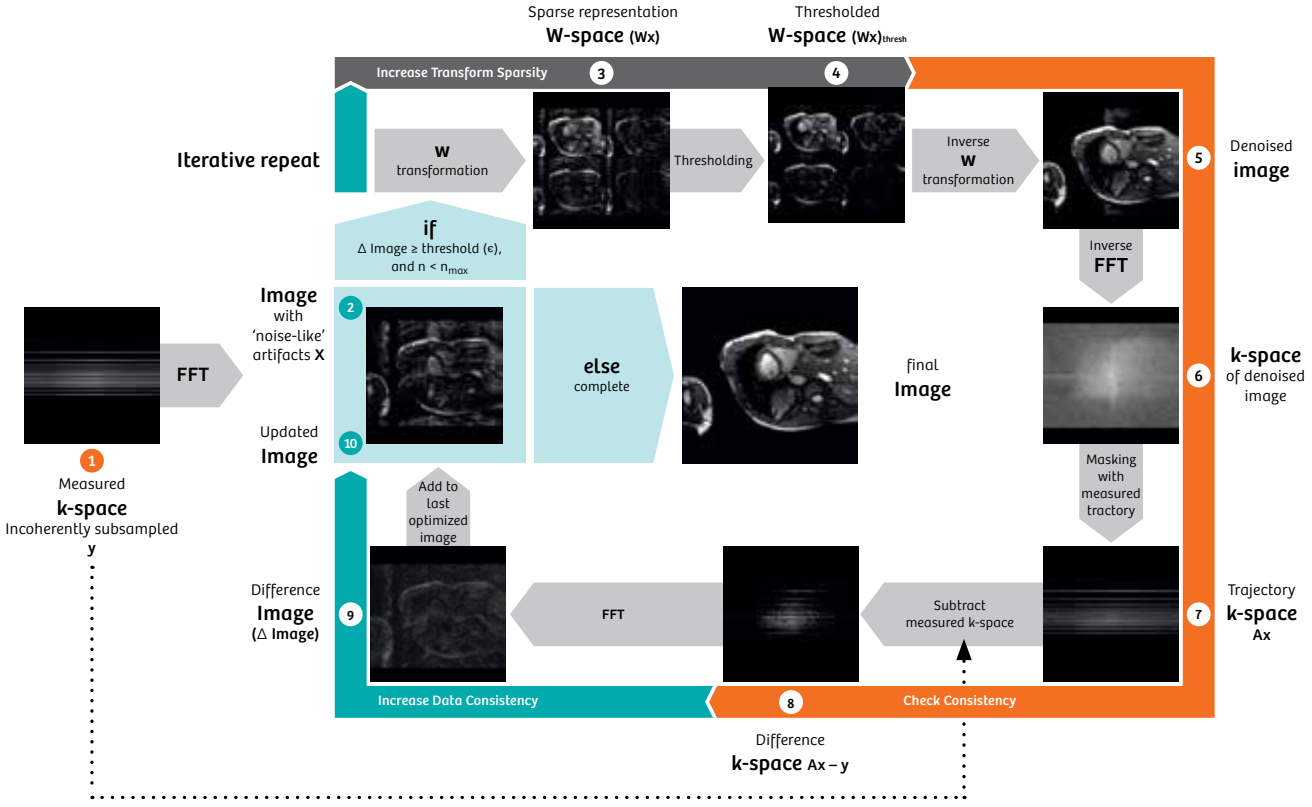

Figure 1. Compressed Sensing Flowchart. Some 'typical' images of the iterative reconstruction are depicted for visualization purposes.

The three key components of Compressed Sensing (CS) are:

1. Incoherent ('random') sub-sampling
2. Transform sparsity
3. Non-linear iterative reconstruction

The Compressed Sensing Flowchart provides a step-by-step visualization of the Compressed Sensing measurement and reconstruction process, explaining where and why these three key components are involved.

Abbreviations and terminology	
k-space **'y'**	Measured data (echoes), sorted in an m x n matrix; in the formulas denoted as **'y'**
Image **'x'**	Clinical image; in the formulas denoted as **'x'**
W-space	Different mathematical depiction of the image Examples: Wavelet, Total Variation
FFT	(Fast) Fourier transformation; transforms k-space into image space
FFT^{-1}	Inverse FFT, transforms image space into k-space
W	W transformation, transforms image space into W-space
W^{-1}	Inverse W Transformation, transforms W-space into image space
A	The transformation A consists of two steps, an inverse FFT and a 'trajectory masking', i.e. only depicting those pixels in k-space that were measured
À	Weighting factor for the tradeoff between data consistency and transform sparcity
$\|\|...\|\|_1$	L1 norm: Sum of all absolute values (here: pixel intensities in W-space)
$\|\|...\|\|_2$	L2 norm, 'Euclidean norm': Square root of sum of squares

The Compressed Sensing optimization formula

The following formula describes the optimization process of CS:

$$\min \| A x - y \|_2^2 + \lambda \| W x \|_1$$

This means that we are searching for an image **x** such that the term above is minimized.

The first term describes the 'data consistency'. It minimizes the least-squares difference (L2 norm, $\|\cdot\|_2^2$) between the estimated image x, and the acquired k-space data y. The smaller this (difference) term becomes, the better the consistency.

The second term describes the 'transform sparsity'. It is the L1 norm of the image transformed into a sparse representation (**W**-space). In this term, the sum of the absolute values of the pixels in the transform domain, denoted by the L1 norm ($\|\cdot\|_1$), is minimized. The smaller this L1 norm, the higher the sparsity. λ is an empirical (application-dependent) weighting factor for balancing data consistency vs. sparsity.

Hence, the optimization procedure minimizing this equation seeks to find a solution that fulfills both criteria, data consistency and transform sparsity. This is done in an iterative process.

1. Measured k-space

The first picture is the measured k-space. There are two differences compared to a 'conventional' scan:

1. Strong sub-sampling, i.e. significantly fewer echoes than in a conventional scan. This results in significantly higher scan speed. But since the Nyquist-Shannon sampling theorem [1] is violated, this will result in strong aliasing artifacts.
2. Incoherent ('random') sampling. This is necessary to create a noise-like appearance of the aliasing artifacts (resulting from the sub-sampling). The reason is that these noise-like artifacts (as opposed to structured artifacts) can then in a later step of the algorithm be removed with a thresholding procedure in W-space (see step 4). The random character of the sampling is essential for the success of the CS reconstruction—"Randomness is too important to be left to chance" [2].

   The incoherent sampling in CS is different from the (typically) coherent sub-sampling that is used in Parallel Acquisition Techniques, where the (structured) aliasing is removed by means of the knowledge of the coil sensitivity profiles.

The k-space in the formula is denoted as **y**.

2. Image

As a first step, the (incoherently) subsampled k-space is Fourier transformed into an image.

This image suffers from strong subsampling artifacts; but these aliasing artifacts are 'smeared' over the image, due to the incoherence of the sampling in step 1. The aliasing artifacts appear 'noise like'. The better the incoherence of the scan, the more 'homogeneous' the noise-like aliasing artifacts will appear, and the better the CS reconstruction will work.

This image serves as a starting point for the iterative optimization. Since we only covered a small part of k-space in step 1, we do not have the complete information about the image. This image **x** generated by a straightforward FFT is only one possible solution that is consistent with the measured data—but this solution suffers from strong artifacts. The following iterative process serves to find a better (artifact-free) solution that is also consistent with the measured data **y**.

The image in the formula is denoted as **x**.

3. W-space

The image is now transformed into a sparse representation (**W**-space). This is a different 'basis', i.e. a different mathematical depiction of the image. The goal of this transformation is to locally separate the 'wanted signal' from the noise (artifacts). **W**-space is a better-suited depiction of the image as the sparsity in **W**-space is higher. This means that the image 'informational content' is concentrated in few pixels in **W**-space, while most pixels have only a very low signal.

There are various different transformations that can be beneficial for this purpose. This depends on the application. A Wavelet transformation is a very common choice for MR imaging.

By the way, a Wavelet transformation is utilized in image compression with the JPEG 2000 format [3].

4. Thresholded W-space

After the **W** transformation (e.g. Wavelet transformation), the 'wanted signal' is now to a high degree separated from the noise (artifacts). This allows removing the noise by a thresholding procedure:

- Set all pixels with a value < threshold to zero;
- Subtract the threshold from all other pixel values.

This procedure is called 'soft thresholding'. It has been shown that 'soft thresholding' is beneficial

for the solution [4]. The threshold is predefined, optimized for the application.

Since many pixels in **W**-space now have a value of 0, we have fewer non-zero pixels (coefficients). The 'transform sparsity', i.e. the sparsity of the image in **W**-space, is increased.

5. Denoised image

We now transform the **W**-space representation back into image space with the inverse **W** transformation ($\mathbf{W}^{-1}$).

By the thresholding procedure in **W**-space in the last step, we have now an image with less noise. This corresponds to a suppression of the noise-like aliasing artifacts, due to the incoherent sampling we applied in step 1.

However, with this denoising we have also 'fiddled' with the image content. The image has less noise (less artifact power) now, but does not exactly reflect the measurement anymore.

In the next steps 6-8, we will therefore check the image consistency (i.e. how well the denoised image still represents the measurement data).

6. k-space of denoised image

In order to compare the denoised image from step 5 with the measured k-space from step 1, we first apply an inverse Fourier Transformation ($\mathbf{FFT}^{-1}$) to transform the image back to k-space.

Since the image in step 6 was modified, its k-space now consists of all spatial frequencies. This means that we have a 'complete k-space' (all pixels in k-space have non-zero values), as opposed to the measured (subsampled) k-space in step 1 which had only few non-zero values.

7. Trajectory k-space

Now follows a masking process. Remember that we measured only a small part of k-space in step 1. The k-space from step 6, on the other hand, is 'complete'. To compare the two, we filter the k-space (step 6) by only depicting the points (the 'measurement trajectory') of k-space (step 6) that were also measured in k-space (step 1). The rest of k-space (step 6) is set to zero.

The two steps inverse FFT (step 6) and masking (step 7) together are called the '**A** matrix' in the formula. The resulting k-space **Ax** can then be directly compared to the measured k-space **y**.

8. Difference k-space

We now create the 'Difference k-space' by subtracting the k-space **Ax** from step 7 from the measured k-space **y** from step 1.

The difference (**Ax – y**) corresponds to the error (non-consistency) that the thresholding from step 4 has created compared to the measured k-space **y**. The difference is a 'correction' k-space, so to speak.

9. Difference image

A simple Fourier transformation converts the 'Difference k-space' into a 'Difference image'.

This is used as a correction for the update of the image that we want to optimize.

10. Updated image

The image **x** from step 2 is now updated by adding the correction (difference) image from step 9.

This updated image now has less noise-like artifacts (corresponding to a higher sparsity in W-space) than the image had before the update, due to steps 3 and 4.

At the same time, it was made consistent with the measured k-space from step 1 by means of the correction from steps 8 to 9.

3-10. Iterative reconstruction

Steps 3 to 10 are now repeated. Each iteration will increase the sparsity (in W-space), corresponding to diminishing the aliasing artifacts in image space. At the same time, the consistency of the reconstruction with the measured k-space is taken care of.

This is an alternating optimization of data consistency and transform sparsity, i.e. the two terms in the formula. The factor λ in the formula is a weighting that defines the trade-off between data consistency and sparsity, it is pre-defined and optimized for the application.

As a metaphor:
One can think of scales rocking to and fro (between the optimization of the first term and the optimization of the second term in the formula). At the same time, the 'center of gravity' (the sum of both terms) is moving down (minimizing both terms in the formula simultaneously). The factor λ in the formula can be thought of as a 'lever', i.e. a shorter (small λ) or longer (large λ) bar of the scales for the sparsity term as compared to the data consistency term.

The iteration of steps 3 to 10 is repeated until:

- either the least-squares difference of the data consistency term, i.e., the Difference Image (step 9), is smaller than a predefined threshold ε,

$$\| Ax - y \|_2^2 < \varepsilon$$

- or a predefined number of iterations N_{max} is reached.

In the end, we will have an image that is consistent with the measured data, but is denoised (i.e. the noise-like aliasing artifacts have been removed) due to the maximization of the transform sparsity. The final image will (very closely) look as if we had measured k-space completely—but at a much shorter scan time.

Optimization of Compressed Sensing

We have seen that there are many degrees of freedom for the optimization of the Compressed Sensing results. All these need to be taken care of in the application development.

The possible CS acceleration factor depends on the transform sparsity of the dataset. If the acceleration factor is chosen too high ("not justified by the sparsity"), the reconstruction will not yield acceptable results. The possible acceleration factor depends on the application.

The weighting factor λ for the balance between transform sparsity vs. data consistency (as described before) and the threshold for the sparsification in W-space (the soft thresholding in the W-space as discussed earlier) are related to each other in order to achieve optimal results. Also these depend on the application.

All the explanations above are a simplification. There are more 'intricacies' that were not discussed for the sake of simplicity, e.g. how the signals from multiple RF channels are handled, the combination of CS with PAT, higher dimensionality, etc.

The CS Flowchart only shows a depiction of a 2D scan (for the sake of simplicity), but Compressed Sensing can also (and better) be applied for multi-dimensional scans

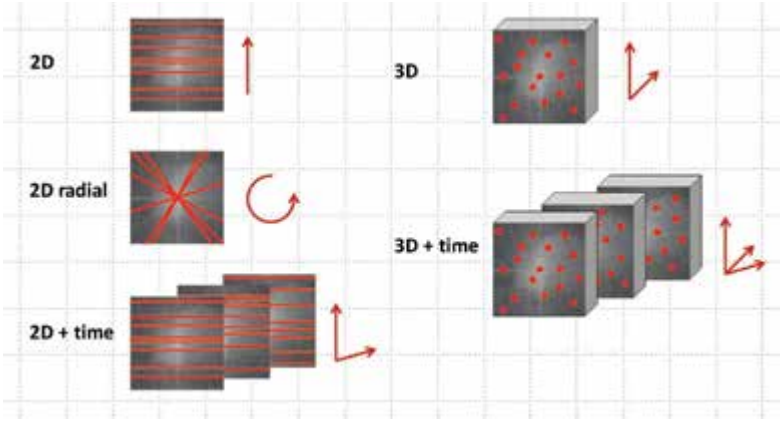

Figure 2. Dimensionality, k-space trajectory and degrees of freedom to improve incoherency ('randomness') of the scan.

with other k-space trajectories. There are two important aspects for the improvement of the CS performance that define which applications benefit most from CS. These are the "Increase of Sparsity" and the "Increase of Randomness".

Increase of Sparsity

An "Increase of Sparsity" will enable higher acceleration factors. If the (transform) sparsity of an MR dataset is low, no significant acceleration will be possible, i.e. it will not be possible to remove the noise-like artifacts while preserving an accurate anatomical depiction. For increasing the possible acceleration factor of the scan, a high 'dimensionality' of the MR scan helps.

A static 2D scan (like a conventional T2-weighted TSE scan) will typically not have a high sparsity (also not in its Wavelet representation). The achievable acceleration with CS for standard static 2D imaging will therefore not be very high.

But it is very different with e.g. Compressed Sensing Cardiac Cine (2D + time). Along the time dimension, the sparsity is quite high. In CS Cardiac Cine, only little changes are expected between sub-sequent time-frames due to the high temporal resolution and the static anatomy surrounding the heart. This increases the transform sparsity along the time dimension, and therefore high accelerations factors (such as 10) can be achieved in CS Cardiac Cine.

Other examples where the dataset has a high dimensionality and therefore higher sparsity with the potential for higher acceleration factors include, for example, 3D scans, dynamic '4D' scans (3D + time) and also diffusion imaging with multiple b-values and or multiple diffusion directions.

Increase of Randomness

Also improving the 'randomness' of the scan will help the performance and the possible acceleration factors of CS.

Figure 2 shows the number of degrees of freedom for different dimensionalities and different k-space trajectories, in order to improve the 'randomness' of the scan.

With static 2D imaging, there is only one degree of freedom, the spacing of the k-space line in phase-encoding direction. The potential for CS acceleration is therefore limited.

With 2D radial imaging, the angle between the different k-space lines can be freely chosen. Each line crosses the center of k-space. There are a couple of advantages for radial imaging vs. cartesian imaging; however, there are also a couple of disadvantages, such as potential aliasing in both directions and longer reconstruction times. The pros and cons of cartesian vs. radial sampling need to be weighed against each other to find the optimal solution, depending on the application.

2D + time (as in Compressed Sensing Cardiac Cine) also has high dimensionality. There are two degrees of freedom, along the phase-encoding direction and along time. The spatial phase-encoding steps can be chosen differently for each cardiac phase.

Static 3D has two degrees of freedom, since there are two phase-encoding directions. This allows a better 'randomness' than static 2D.

Dynamic 3D has an additional degree of freedom, along time. This high dimensionality of course holds great promise for future developments, already available as WIP packages from Siemens Healthineers.

Overall, there is a wide potential for future Compressed Sensing applications with high acceleration factors and high clinical relevance.

References

[1]https://en.wikipedia.org/wiki/Nyquist%E2%80%93Shannon_sampling_theorem

[2]Marseille GJ, de Beer R, Fuderer M, Mehlkopf AF, van Ormondt D. Nonuniform phase-encode distributions for MRI scan time reduction. J Magn Reson 1996;111:70–75

[3]https://en.wikipedia.org/wiki/JPEG_2000

[4]David L. Donoho, De-noising by Soft-Thresholding, http://statweb.stanford.edu/~donoho/Reports/1992/denoiserelease3.pdf

Contact
Mathias Blasche
Mathias.Blasche@siemens-healthineers.com

Compressed Sensing—a Paradigm Shift in MRI

Christoph Forman[1]; Jens Wetzl[2]; Carmel Hayes[1]; Michaela Schmidt[1]
[1]Siemens Healthineers, Magnetic Resonance, Erlangen, Germany
[2]Pattern Recognition Lab, Friedrich-Alexander-University Erlangen-Nuremberg, Erlangen, Germany

Introduction

Reducing the complexity and length of examinations has been a major direction of research in magnetic resonance imaging (MRI) in recent years. With the introduction of the Dot engines, the complexity of MR examinations could be reduced through automatization and guidance, providing standardized and time-efficient workflows. Considerable effort has also been spent on developing methods to speed up data acquisition without degrading image quality. Accelerated imaging is a key factor to enable the visualization of rapid physiological or contrast changes in dynamic imaging. Moreover, short scans reduce the risk of artifacts due to any kind of motion during the scan. A significant speed-up of data acquisition allows both respiratory and cardiac motion to be frozen while maintaining an adequate temporal and spatial resolution. This in turn results in a high-quality and robust examination even for uncooperative patients, since data acquisition may be performed in free-breathing. Furthermore, reduced scan time and a decreased number of breath-holds improve patient comfort. Last but not least, accelerated imaging means shorter examinations that can be invested in additional scans, higher resolution, or to improve the overall patient throughput. In this context, parallel imaging and compressed sensing techniques have been proposed to significantly speed up the acquisition time while maintaining diagnostic image quality.

Parallel imaging

Parallel imaging [1, 2] is well established in current clinical practice to speed up data acquisition

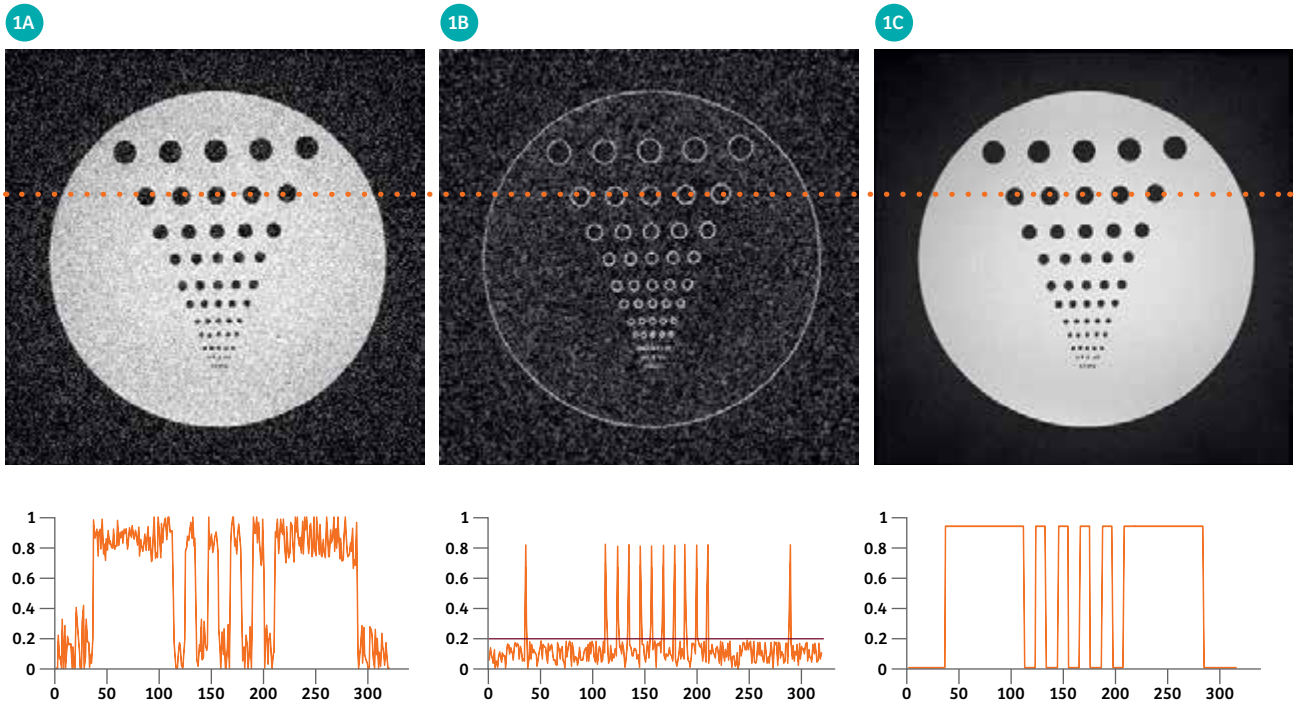

Figure 1. Additional noise reduces the homogeneity in the image of the resolution phantom **(1A)**, which can also be observed in the line plot along the dashed line. After transformation into a sparse representation using finite differences **(1B)**, the homogeneity can be restored by denoising, i.e., setting all pixels below a threshold level (red line) to 0. After the image is transformed back to its original domain, the phantom is piecewise constant **(1C)**.

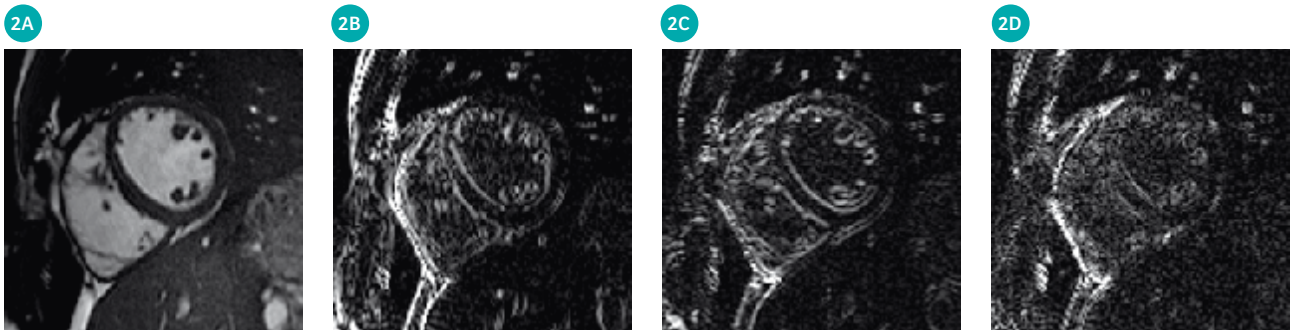

Figure 2. The short-axis view of the heart **(2A)** is transformed by the wavelet transform to achieve a sparse representation. In addition to the low-resolution representation of the original image, the wavelet transform results in three edge images **(2B-2D)**: While **(2B)** and **(2C)** contain the edges in horizontal and vertical direction, respectively, Figure 2D shows the diagonal edge components of the image. In the wavelet domain, the content of the image is sufficiently described by only few coefficients, i.e. the bright pixels.

in a large number of applications. With this technique, scan acceleration is usually achieved by uniformly sub-sampling ***k***-space, for example, by skipping every other line. The resulting aliasing can be unfolded by incorporating the spatial encoding capabilities of multi-coil receiver arrays. However, the scan time reduction is often restricted to moderate acceleration factors between 2 and 4. This limitation is due to the restricted encoding capabilities in terms of number and position of the receiver coils. Additionally, acquiring less data also leads to a reduced signal-to-noise ratio (SNR).

Compressed sensing

In recent years, compressed sensing has gained large scientific attention. Originally, it was proposed as a general concept to accurately reconstruct a signal from a small number of random measurements [3,4]. A few years later, compressed sensing was introduced to MRI [5] and successfully combined with parallel imaging [6]. Exploiting the *compressibility* of medical images, this method promises to markedly exceed the acceleration rates that are feasible with parallel imaging. Although compressed sensing has denoising properties, it also has to deal with SNR loss from scan acceleration. Hence, possible acceleration factors scale with the native SNR of the scan. Up to now, the potential of compressed sensing has been shown in a large number of applications from 2D to 5D imaging [7-15].

The successful utilization of compressed sensing is a team play of data acquisition and image reconstruction. In the paper introducing compressed sensing to MRI, three criteria were identified as being essential to ensure successful image recovery from sub-sampled data [5]:

- First, the object that is acquired should have a sparse representation after conversion with a mathematical transformation.
- Second, ***k***-space should be sub-sampled such that the aliasing results in incoherent, i.e. noise-like, artifacts in the image.
- Finally, image reconstruction requires a nonlinear, iterative optimization that simultaneously enforces a sparse representation of the resulting image. Thereby, it removes the noise-like artifacts, while it preserves its consistency to the acquired data.

These three essential requirements are discussed in detail below.

Transform sparsity

An image is considered as sparse when its informational content is represented by only a few pixels, while the contribution of the remaining majority of pixels is close to zero. In medical imaging, an angiogram provides a good example for such a sparse representation. However, in MRI, not all images are inherently sparse. But these images can also have a sparse representation utilizing a sparsifying transform. This transform provides an invertible mapping from an image to a sparse representation. Finite differences, i.e. images that contain only edge information, provide a simple technique to achieve a sparse representation, if the image is piecewise constant as shown in Figure 1. Discrete cosine transform and discrete wavelet transform are frequently used in the context of image compression, for example, in JPEG image compression. Utilizing such methods, images may be

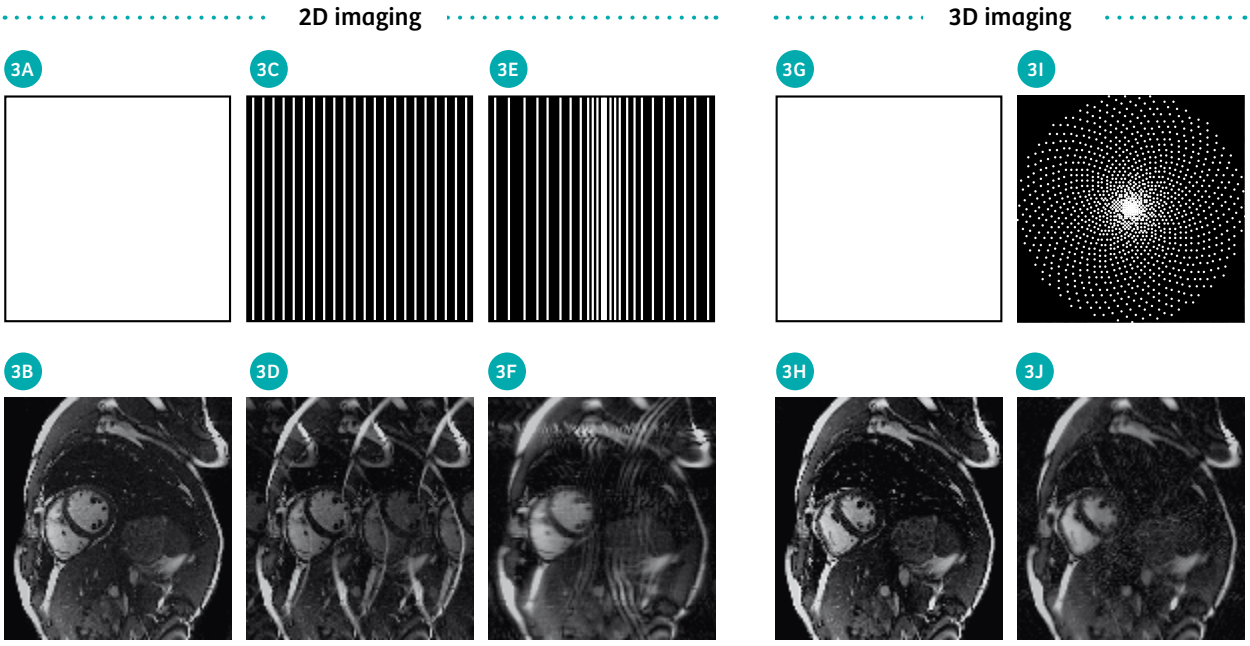

Figure 3. Examples of different sampling schemes, where ***k***-space locations that are acquired are highlighted in white and the ones that are skipped are black (upper row) with corresponding image results and aliasing artifacts after Fourier transform (lower row). In 2D imaging, sub-sampling is limited to one phase-encoding direction whereas for 3D sub-sampling can be applied in two phase-encode directions. In case of CINE imaging, additional incoherence can be achieved in the temporal domain. **(3A, 3B)** Fully sampled ***k***-space with artifact free result image; **(3C, 3D)** Regular subsampled ***k***-space like PAT resulting in superposition of multiple ghosts; **(3E, 3F)** Irregular subsampled ***k***-space as used in CS leading to incoherent aliasing artifacts similar to noise; **(3G, 3H)** Fully sampled ***k***-space with artifact free result image; **(3I, 3J)** Irregular subsampled ***k***-space as used in CS with noise-like artifacts.

transformed into a sparse representation (see Fig. 2). In this domain, the content of the image is sufficiently described by only few coefficients, i.e. the bright pixels. The percentage of these pixels relative to the total number of pixels defines the sparsity of the image. For image compression, pixels in this sparse representation that are below a certain threshold can be set to zero, which facilitates a compression of the signal. Once the compressed signal is converted back to its initial domain, the visual difference between the resulting image and its original version is negligible. In particular, the discrete wavelet transform has been shown to be a suitable sparsifying transform for many natural images, including MRI images, and is commonly used in compressed sensing applications. In the case of dynamic imaging, including CINE imaging, this transform can also be applied in the temporal dimension. The redundancy of information along this temporal dimension can be exploited, and often the sparsity is even higher compared to the spatial dimensions.

Incoherent sampling

Unlike the regular sub-sampling patterns used for parallel imaging, the data acquisition process for compressed sensing requires that ***k***-space sub-sampling is irregular (see Fig. 3C for regular and 3E, 3I for irregular sampling). In conventional Cartesian parallel imaging, regular sub-sampling of ***k***-space is advantageous in that the phase-encoding gradient is increasing linearly during the measurement, which is beneficial for physical and MRI hardware limitation reasons. However, violating the Nyquist sampling theorem in this manner results in a superposition of shifted replicas of the original signal as illustrated in Figure 3D. The number of replicas equals the chosen sub-sampling rate. This aliasing can then be unfolded utilizing the spatial encoding capabilities of the multi-coil receiver array and parallel imaging. In contrast, irregular, incoherent sub-sampling of ***k***-space, as required for compressed sensing, would result in a noise-like appearance of sub-sampling artifacts (see Figs. 3F, 3J). Theoretically, completely random sub-sampling is optimal to ensure this noise-like behavior. However, purely random sampling is impractical in the case of MRI.

On the one hand, large and random steps in ***k***-space may require large-amplitude gradient steps and should be avoided due to hardware limitations and physical reasons. On the other hand, the sampling trajectory must be repeatable to allow the same acquisition to be

reproduced with consistent image quality. Therefore, sub-sampling patterns featuring deterministic properties that mimic random sampling within the given constraints are frequently used for compressed sensing data acquisition. In 2D Cartesian imaging with pure spatial coverage, the sub-sampling is limited to one dimension, as only the phase-encoding direction is sub-sampled in MRI. But in case of 2D dynamic imaging, the sampling pattern can be varied from one time frame to the next in order to maintain sufficient incoherence for compressed sensing. In 3D Cartesian imaging, sub-sampling can be applied in two phase-encoding directions. Alternatively, non-Cartesian sampling trajectories can be used, e.g., radial or spiral imaging, that already facilitate an incoherent sampling of ***k***-space for 2D imaging.

Nonlinear image reconstruction

If the two above-mentioned requirements are sufficiently met, the image can be recovered from the sub-sampled data by nonlinear, iterative reconstruction. In this reconstruction, a data fidelity term ensures consistency of the estimated image to the acquired data and a transform sparsity term enforces a sparse representation of the image in the transform domain by solving the following equation:

$$\min_{x} \underbrace{\|Ax-y\|_2^2}_{\text{data fidelity}} + \lambda \underbrace{\|\Phi(x)\|_1}_{\text{transform sparsity}}$$

The data fidelity term minimizes the least-squares difference ($\|\cdot\|_2^2$) between the estimated image, x, and the acquired ***k***-space data, y. The system matrix, A, describes the data acquisition process, i.e., the transform from spatio-temporal to frequency domain, which is required for the comparison of the image and acquired data. Incorporating parallel imaging, it consists of the coil sensitivity maps of the individual receiver coil elements, the Fourier transform, and the applied sub-sampling pattern during data acquisition. In the transform sparsity term, the image is transformed into a sparse representation by $\Phi(\cdot)$, for example, using the discrete wavelet transform. In this term, the sum of the absolute values of the pixels in the transform domain, denoted by the ℓ_1 norm ($\|\cdot\|_1$), is minimized. Hence, the optimization procedure minimizing this equation seeks to find a solution that fulfills both criteria, data consistency and transform sparsity. This optimization procedure is more computationally intensive than conventional reconstruction, e.g., parallel imaging. The balance between data fidelity and sparsity is adjusted with the regularization parameter λ, which is usually found empirically. While small values of λ lead to an image that is closer to the acquired data, increasing this value tends to produce an image that is in favor of the sparse solution. When λ is too low, the image will be noisy, and when λ is too high a strongly filtered image appearance may be the consequence. The equation described above is iteratively minimized until a convergence criterion is met or a fixed number of iterations is reached. Figure 4 illustrates this optimization in the example of real-time CINE imaging of the heart.

Transition into clinical routine

Compressed sensing acquisition and reconstruction have been completely integrated into our clinical MRI scanners. Works-in-progress packages have been developed and tested by our clinical cooperation partners world-wide for various applications in the fields of cardiovascular [16-19], neurological [20], musculoskeletal [21-23] and oncological[24] imaging. The additional parameters needed to compose the compressed sensing protocols, for both acquisition and reconstruction, have been seamlessly integrated into our user interface (UI). A selection of possible continuous acceleration factors takes the place of discrete numbers that were familiar from parallel imaging. This facilitates a UI experience with a low level of complexity. The award-winning algorithm for compressed sensing reconstruction [8], ranking first at the ISMRM 2014 "sub-Nyquist" reconstruction challenge, has been fully integrated into the Siemens Healthineers image reconstruction environment. Without the need for additional hardware, the images are directly calculated inline utilizing the full computational power of the reconstruction computer. Compressed sensing reconstruction is performed on a graphics processing unit, which provides a significant speed-up in processing time. For example, the image series of one cardiac real-time CINE slice is processed in 10 to 15 seconds.

Thanks to its high acceleration rate due to compressed sensing, real-time sequences allow for a temporal and spatial resolution comparable to that of conventional segmented acquisitions. For example, compressed sensing in cardiac imaging permits fast quantification of left-ventricular (LV) function in a single breath-hold [25]. As demonstrated in Figure 5, this sequence still provides diagnostic images for LV function quantification even in challenging scenarios, such as in the presence of arrhythmia, where conventional sequences usually fail. This sequence may also be applied in free-breathing, which

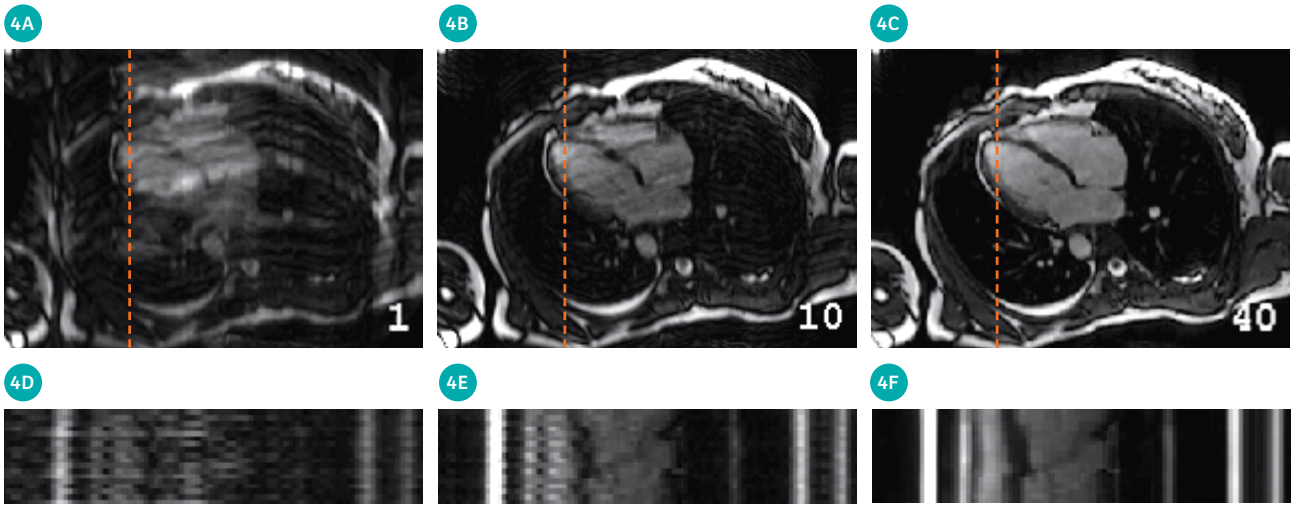

Figure 4. This Figure shows the progress of the optimization procedure to preserve data fidelity and reduce noise-like artifacts exemplarily in a Cardiac 2D CINE dataset **(4A-4C)**. While the top image shows one image of the time series, a temporal profile along the dashed line is plotted below. The incoherent sub-sampling in the spatio-temporal domain results in incoherent artifacts that dominate the image after the first iteration **(4A)**. Enforcing a sparse representation of the image and exploiting temporal redundancy, these artifacts are reduced with an increasing number of iterations **(4B)**. The compressed sensing reconstruction is terminated after 40 iterations and results in an aliasing-free image **(4C)**.

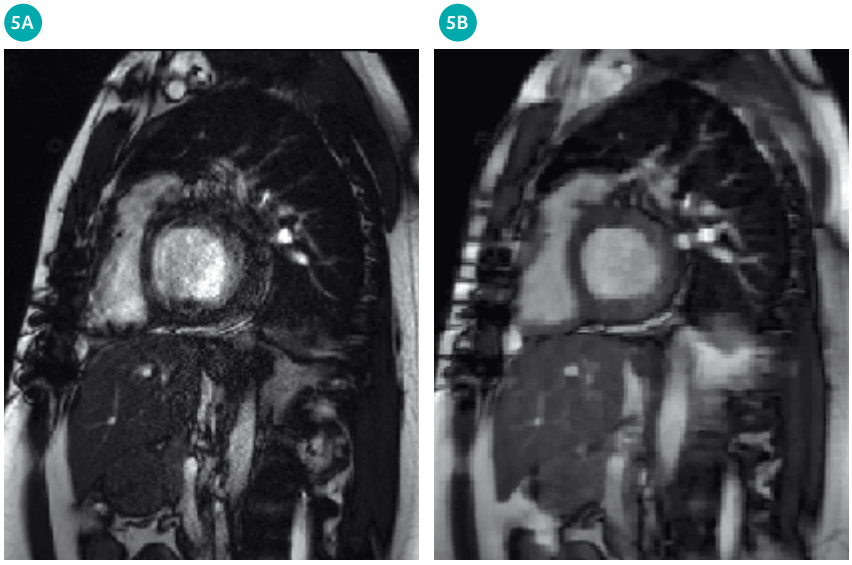

Figure 5. In cardiac imaging, the high acceleration rate due to compressed sensing enables real-time CINE imaging with a temporal and spatial resolution in a comparable range as conventional segmented acquisitions. While conventional imaging might fail in challenging scenarios, like in case of arrhythmia **(5A)**, the compressed sensing real-time sequence preserves a diagnostic image quality that still enables the quantification of LV function **(5B)**.

Images courtesy of Dr. François Pontana, Lille University Hospital, Lille, France.

is beneficial for patients who are not able to hold their breath sufficiently and, in general, allows for a simplified and more patient-friendly examination workflow.

Conclusion

Compressed sensing facilitates rapid MR imaging by exploiting the fact that medical images have a sparse representation in a certain transfer domain. Representing a team play of data acquisition and image reconstruction, this allows for the reconstruction of artifact-free images following incoherent data acquisition. The acceleration enables a reduction in the acquisition time or an improvement in the spatial and/or temporal resolution. Real-time imaging featuring compressed sensing helps to reduce the need for breath-holding or ECG triggering. The integration of protocols based on compressed sensing in clinical workflows allows a significant reduction in the examination time for each patient. Our generalized integration of compressed sensing in the scanner environment will allow for the straightforward introduction of further applications that are likely to come in the near future.

References

[1] M. A. Griswold, P. M. Jakob, R. M. Heidemann, M. Nittka, V. Jellus, J. Wang, B. Kiefer, and A. Haase. "Generalized Autocalibrating Partially Parallel Acquisitions (GRAPPA)". Magnetic Resonance in Medicine, Vol. 47, No. 6, pp. 1202–1210, June 2002.

[2]K. Pruessmann, M. Weiger, M. B. Scheidegger, and P. Boesiger. "SENSE: Sensitivity Encoding for Fast MRI". Magnetic Resonance in Medicine, Vol. 42, No. 5, pp. 952–962, Nov. 1999.

[3]D. Donoho. "Compressed Sensing". IEEE Transactions on Information Theory, Vol. 52, No. 4, pp. 1289–1306, Apr. 2006.

[4]E. Candes and J. Romberg. "Sparsity and incoherence in compressive sampling". Inverse problems, Vol. 23, No. 3, pp. 969–985, Apr. 2007.

[5]M. Lustig, D. Donoho, and J. M. Pauly. "Sparse MRI: The Application of Compressed Sensing for Rapid MR Imaging". Magnetic Resonance in Medicine, Vol. 58, No. 6, pp. 1182–1195, Dec. 2007.

[6]D. Liang, B. Liu, J. Wang, and L. Ying. "Accelerating SENSE Using Compressed Sensing". Magnetic Resonance in Medicine, Vol. 62, No. 6, pp. 1574–1584, Dec. 2009.

[7]G. Adluru, L. Chen, S. Kim, N. Burgon, E. G. Kholmovski, N. F. Marrouche, and E. V. R. DiBella. "Three-dimensional late gadolinium enhancement imaging of the left atrium with a hybrid radial acquisition and compressed sensing". Journal of Magnetic Resonance Imaging, Vol. 34, No. 6, pp. 1465-1471, Dec. 2011.

[8]J. Liu, J. Rapin, T.-C. Chang, A. Lefebvre, M. O. Zenge, E. Mueller, and M. S. Nadar. "Dynamic cardiac MRI reconstruction with weighted redundant Haar wavelets". In: Proceedings of the 20th Annual Meeting of ISMRM, p. 4249, Melbourne, Australia, May 2012.

[9]F. Han, S. Rapacchi, S. Kahn, I. Ayad, I. Salusky, S. Gabriel, A. Plotnik, J. P. Finn, and P. Hu, "Four-dimensional, multiphase, steady-state imaging with contrast enhancement (MUSIC) in the heart: A feasibility study in children". Magnetic Resonance in Medicine, Vol. 74, No. 4, pp. 1042-1049, Oct. 2015.

[10]S. T. Ting, R. Ahmad, N. Jin, J. Craft, J. Serafim da Silveira, H. Xue, and O. P. Simonetti. "Fast Implementation for Compressive Recovery of Highly Accelerated Cardiac Cine MRI Using the Balanced Sparse Model". Magnetic Resonance in Medicine, doi: 10.1002/mrm.26224.

[11]D. Stäb, T. Wech, F. A. Breuer, A. M. Weng, C. O. Ritter, D. Hahn, and H. Köstler, "High resolution myocardial first-pass perfusion imaging with extended anatomic coverage". Journal of Magnetic Resonance Imaging, Vol. 39, No. 6, pp. 1575–1587, Jun. 2014.

[12]X. Chen, M. Salerno, Y. Yang, and F. H. Epstein, "Motion-compensated compressed sensing for dynamic contrast-enhanced MRI using regional spatiotemporal sparsity and region tracking: Block low-rank sparsity with motion-guidance (BLOSM)", Magnetic Resonance in Medicine, Vol. 72, No. 4, pp. 1028-1038, Oct 2014.

[13]H. Xue, S. Inati, S. Sørensen, P. Kellman, and M. S. Hansen, "Distributed MRI Reconstruction Using Gadgetron-Based Cloud Computing", Magnetic Resonance in Medicine, Vol. 73, No. 3, pp. 1015-1025, March 2015.

[14]J. Wetzl, F. Lugauer, M. Schmidt, A. Maier, J. Hornegger, and C. Forman. "Free-Breathing, Self-Navigated Isotropic 3-D CINE Imaging of the Whole Heart Using Cartesian Sampling", In: Proceedings of the 24th Annual Meeting of ISMRM, p. 411, Singapore, May 2016.

[15]L. Feng, L. Axel, H. Chandarana, K. T. Block, D. K. Sodickson, and R. Otazo. "XD-GRASP: Golden-angle radial MRI with reconstruction of extra motion-state dimensions using compressed sensing". Magnetic Resonance in Medicine, Vol. 75, No. 2, pp. 775–788, Feb. 2016.

[16]C. Forman, D. Piccini, R. Grimm, J. Hutter, J. Hornegger, and M.O. Zenge. "Reduction of respiratory motion artifacts for free-breathing whole-heart coronary MRA by weighted iterative reconstruction", Magnetic Resonance in Medicine, Vol. 73, No. 5, pp. 1885-1895, May 2015.

[17]A. F. Stalder, M. Schmidt, H. H. Quick, M. Schlamann, S. Maderwald, P. Schmitt, Q. Wang, M. S. Nadar, and M. O. Zenge. "Highly undersampled contrast-enhanced MRA with iterative reconstruction: Integration in a clinical setting", Magnetic Resonance in Medicine, Vol. 74, No. 6, pp. 1652-1660, Dec. 2015

[18]T. Yamamoto, K. Fujimoto, T. Okada, Y. Fushimi, A. Stalder, Y. Natsuaki, M. Schmidt, and K Togashi, "Time-of-Flight Magnetic Resonance Angiography With Sparse Undersampling and Iterative Reconstruction: Comparison With Conventional Parallel Imaging for Accelerated Imaging", Investigative Radiology, Vol. 51, No. 6, pp. 372-378, Jun 2016.

[19]J. Wetzl, C. Forman, B. J. Wintersperger, L. D'Errico, M. Schmidt, B. Mailhe, A. Maier, and A. F. Stalder. "High-resolution dynamic CE-MRA of the thorax enabled by iterative TWIST reconstruction", Magnetic Resonance in Medicine, doi: 10.1002/mrm.26146.

[20]E. Mussard, T. Hilbert, R. Meuli, J.-P. Thiran, and T. Kober. "Accelerated MP2RAGE Imaging Using Sparse Iterative Reconstruction", In: Proceedings of the 24th Annual Meeting of ISMRM, p. 4216, Singapore, May 2016.

[21]R. Otazo, M. Nittka, M. Bruno, E. Raithel, C. Geppert, S. Gyftopoulos, M. Recht, and L. Rybak. "Sparse-SEMAC: Rapid and Improved SEMAC Metal Implant Imaging Using SPARSE-SENSE Acceleration", Magnetic Resonance Imaging, July 2016, Early View, DOI: 10.1002/mrm.26342.

[22]J. Fritz, S. Ahlawat, S. Demehri, G.K. Thawait, E. Raithel, W.D. Gilson, M. Nittka. "Compressed Sensing SEMAC: 8-fold Accelerated High Resolution Metal Artifact Reduction MRI of Cobalt-Chromium Knee Arthroplasty Implants", Investigative Radiology, October 2016, Vol. 51, Issue 10, pp 666–676.

[23]J. Fritz, E. Raithel, G. K. Thawait, W. Gilson, and D. F. Papp. "Six-Fold Acceleration of High-Spatial Resolution 3D SPACE MRI of the Knee Through Incoherent k-Space Undersampling and Iterative Reconstruction – First Experience". Investigative Radiology, Vol. 51, No. 6, pp. 400-409, Jun 2016.

[24]D. Nickel, X. Chen, B. Mailhe, Q. Wang, Y. Son, J. M. Lee, and B. Kiefer. "Motion-resolved 3D dynamic contrast enhanced liver MRI", In: Proceedings of the 24th Annual Meeting of ISMRM, p. 4253, Singapore, May 2016.

[25]G. Vincenti, P. Monney, J. Chaptinel, T. Rutz, S. Coppo, M.O. Zenge, M. Schmidt, M.S. Nadar, D. Piccini, P. Chèvre, M. Stuber, and J. Schwitter, "Compressed Sensing Single–Breath-Hold CMR for Fast Quantification of LV Function, Volumes, and Mass" JACC: Cardiovascular Imaging, Vol. 7, No. 9, pp. 882–892, Sep. 2014.

Contact
Christoph Forman
christoph.forman@siemens-healthineers.com

Compressed Sensing—a Metaphor

Mathias Blasche
Siemens Healthineers, Erlangen, Germany

Compressed Sensing (CS) is an exciting new method with the potential to accelerate MR scans beyond what is possible with any other method. However, the CS reconstruction method is more complicated than the straight-forward Fourier transform used in conventional MR imaging.

The three key components of CS—incoherent sub-sampling, transform sparsity, and iterative reconstruction—may sound 'unwieldy' to many readers.

The 'Washing Metaphor' described below compares the CS mechanism with the washing of a T-shirt. This might look a little funny (and in fact this is intended), but it is actually quite an accurate analogy. It might help understanding CS in a 'non-technical' sort of way. Enjoy!

The goal of Compressed Sensing is to remove the (noise-like) aliasing artifacts from the image (that are due to the incoherent sub-sampling of the measured *k*-space) while ensuring that the reconstructed image is still consistent with the measured data.

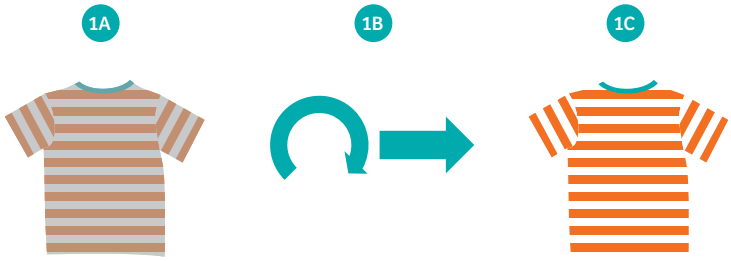

1

Goal of Compressed Sensing	
(1A) MRI: We measure only a part of *k*-space (sub-sampling) in an incoherent ('random') way. This results in an image with noise-like aliasing artifacts.	**Metaphor:** We have a dirty T-shirt[1]. The dirt is homogeneously grey.
(1B) MRI: By maximizing transform sparsity[2], we remove the noise (= the aliasing artifacts) from the image. We take care that we keep the reconstructed image consistent with the measured data. The simultaneous improvement of sparsity and data consistency is done in an alternating fashion, iteratively until the optimum is achieved.	**Metaphor:** We wash the T-shirt in the rotating tub of the washing machine to remove the grey dirt. We take care not to wash out the colors.
(1C) MRI: The result is an anatomically correct image without aliasing artifacts (noise). The image looks virtually identical to an image with a completely measured *k*-space—but at much shorter scan time.	**Metaphor:** The T-shirt is clean, and the colors have been preserved. The T-shirt looks like new.

[1]*Note: The red-white striped T-shirt was chosen as an arbitrary example. The stripes have nothing to do with any 'regular' sampling of k-space.*
[2]*'Sparsity' stands for 'transform sparsity' in the remainder of the text, i.e. the sparsity in W-space, e.g. the Wavelet domain. Increasing sparsity in W-space corresponds to decreasing noise in image space.*

In order to achieve the optimal result, the sum of sparsity and data consistency is maximized. This corresponds to a minimization of noise (= aliasing artifacts) while keeping anatomical accuracy. The sparsity needs to be optimally balanced with respect to the data consistency.

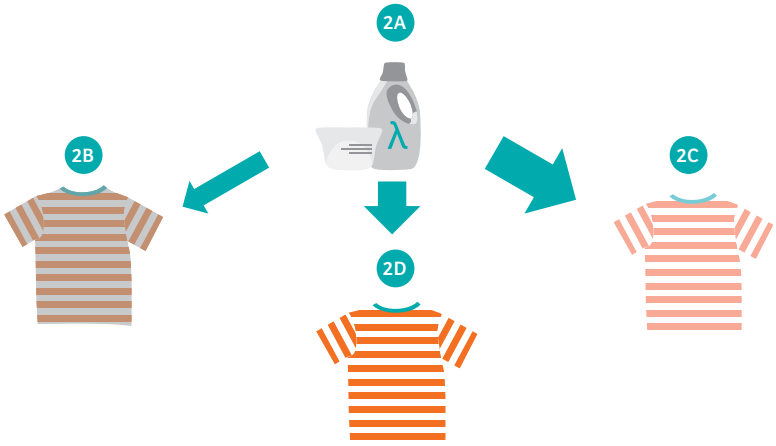

2 Sparsity vs. Data Consistency

(2A) For optimal balancing between sparsity and data consistency, the correct weighting factor λ needs to be applied. λ is application dependent and is optimized during the application development.[3]	**Metaphor:** The right amount of detergent has to be used.
(2B) MRI: If the sparsity weighting is too low (λ too small), there is still noise (aliasing artifacts) in the image.	**Metaphor:** With too little detergent, we will not remove the dirt on the T-shirt.
(2C) MRI: If the sparsity weighting is too high (λ too large), we will lose data consistency. The image is noise free but it does not show the true anatomy.	**Metaphor:** Using too much detergent, the dirt will be gone— but also the colors.
(2D) MRI: The right balance between sparsity and data consistency (optimal λ) results in the anatomy being depicted correctly, without noise (aliasing artifacts). The image looks as if we had measured ***k***-space completely – but at much shorter scan time.	**Metaphor:** With the right amount of detergent, the dirt can be removed without affecting the colors. The T-shirt looks like new.

[3]To avoid misunderstandings: λ is preset, it is optimized for the application. It is not changed in the iterative reconstruction. Rather, the iterative reconstruction improves data consistency and sparsity in an alternating fashion, based on the preset λ.

Finally, we want to emphasize again the importance of incoherent ('random') scanning for a successful CS reconstruction.

3 The Importance of Incoherent Scanning

3A) MRI: In case we do not sample ***k***-space 'randomly enough', the aliasing artifacts will appear in a discrete way and not noise-like. Without this critical prerequisite for CS, the reconstruction will fail[4].	**Metaphor:** If we have concentrated stains instead of 'homogeneous dirt', it will not be possible to wash the stains off without destroying the colors.
(3B) MRI: If we concentrate on data consistency, we will not get rid of the artifacts (which are not noise-like but discrete).	**Metaphor:** If we concentrate on not washing off the colors (by using a low amount of detergent), we will not succeed in removing the concentrated stains completely.
(3C) MRI: If we emphasize sparsity (complete removal of the discrete high-intensity aliasing artifacts which are not noise-like), this will go at the expense of data consistency. The anatomy is not depicted correctly.	**Metaphor:** If we use enough detergent to wash off the stains, the colors will also fade out.

[4] *For the sake of simplicity, we are discussing a pure CS reconstruction without the combination with parallel imaging. The combination with parallel imaging would also address discrete aliasing artifacts to a certain degree.*

Exercise Cardiac MRI, a Clinical Reality with Compressed Sensing

Wendy Strugnell, BAppSc(MIT) FSMRT; Aaron Lin, MBChB, FRACP
Richard Slaughter Centre of Excellence in Cardiovascular MRI
The Prince Charles Hospital, Brisbane, Australia

Introduction

Non-invasive assessment of ventricular function plays an important role in the diagnosis and management of cardiac diseases. With its high temporal and spatial resolution, cardiac MRI is considered the most accurate non-invasive tool for providing left ventricular (LV) volumes, ejection fraction (EF) and mass at rest [1-3]. Cardiac MRI is also superior to other imaging modalities for quantitative assessment of the complexly shaped right ventricle (RV) [4-6].

Due to practical and technical limitations of imaging, clinical cardiac assessment is conventionally performed with the patient at rest. However, in many heart diseases, symptoms do not occur at rest and ventricular assessment during exercise is necessary to unmask ventricular dysfunction that is not apparent at rest. Despite recent technological advances across imaging modalities, assessment of dynamic ventricular response during exercise remains challenging. Until now, non-invasive quantitative cardiac assessment during exercise has been performed using echocardiography and nuclear scintigraphy, both of which have significant limitations, particularly in the assessment of the RV. As MRI is superior to other imaging modalities in accuracy and reproducibility of ventricular functional results at rest, there is a clinical need for a reliable MRI assessment of the heart during exercise.

Limitations of cardiac MRI during exercise

Quantitative MRI assessment of cardiac function requires the acquisition of a stack of ECG-gated, cine ventricular short-axis images [5]. This time-consuming process requires multiple breath-holds to cover the entire ventricle and can be difficult for some patients to complete. This process can be made more challenging by exercise, particularly in patients with cardiac and pulmonary diseases whose baseline exercise and respiratory capacities are limited.

These limitations have driven the search for faster imaging techniques that maintain acceptable image quality and temporal resolution from resting heart rates through to accelerated heart rates during exercise. Real-time MRI is less susceptible to motion caused either by exercising or breathing and can be performed without ECG gating. La Gerche et al. [7] recently demonstrated that when real-time ungated MRI is combined with *post hoc* analysis incorporating compensation for respiratory motion, accurate biventricular volumes could be measured during maximal exercise. However, the methodology is labor intensive with lengthy post-processing times, and the authors acknowledge that there is significant difficulty in identifying the endocardium at higher levels of exercise. Access to commercially

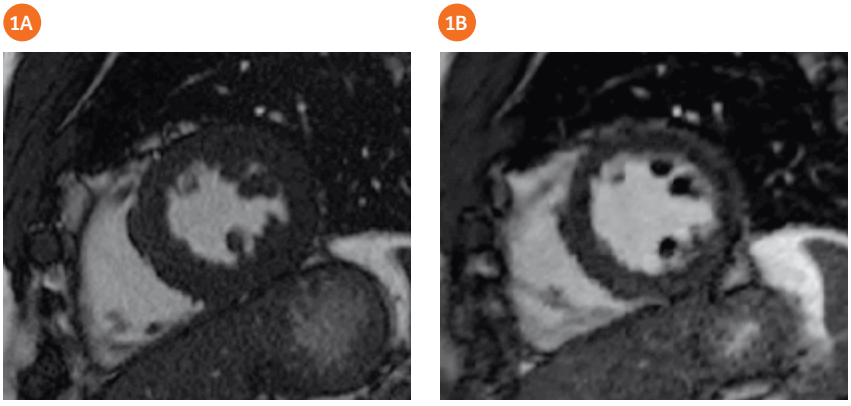

Figure 1. Midventricular short-axis images at end-distole from the conventional bSSFP acquisition (acceleration factor 2) **(1A)** and the high spatial and temporal resolution CS_bSSFP acquisition (acceleration factor 8) **(1B)**, from the same patient.

available processing software to enable analysis is another major limitation of this technique. Most real-time sequences also have low temporal resolution, which may affect accuracy at the high heart rates encountered during exercise. Clearly, the pursuit for a fast, clinically feasible MRI technique for evaluating the ventricles during exercise remains.

Compressed Sensing MRI

Compressed Sensing (CS) was recently proposed as a means to considerably accelerate data acquisition through sparse sampling and reconstructing signals or images from significantly fewer measurements than were traditionally thought necessary [8-9]. Using incoherent sparse sampling, nonlinear reconstruction algorithms and iterative processing, these methods reconstruct undersampled data from significantly fewer measurements whilst maintaining in-plane spatial resolution [10]. Cardiac MRI is ideally suited to CS techniques. Vincenti et al. [11] demonstrated that the application of CS to cardiac imaging enabled several-fold acceleration and achieved a cine acquisition of the whole heart in one breath-hold.

With local institutional review board approval, we recently tested a prototype, ECG-triggered balanced steady-state free precession cine sequence with compressed sensing (CS_bSSFP)* (net acceleration of 8) against the conventional bSSFP sequence (net acceleration of 2) on clinical patients using comparable parameters for spatial and temporal resolution. We concluded that accurate and reproducible volumetric quantifications equaling those of conventional bSSFP could be achieved in the assessment of the left ventricle at rest in various cardiac disease states at significantly shorter acquisition times [12] (Fig. 1).

Exercise cardiac MRI

Patients with cardiac and pulmonary diseases typically have limited exercise tolerance and breath-hold capacity. Quantitation of ventricular function by cardiac MRI during exercise requires:

1. Fast acquisition covering the whole ventricle to avoid fatigue from exercise (maximum total exercise time 15 minutes);

Table 1. Imaging parameters of conventional bSSFP and CS_bSSFP1 sequences.

	bSSFP	CS_bSSFP1
TR (ms)	3	2.53
TE (ms)	1.25	1
Field-of-view (mm)	380 x 290	380 x 312
Image Matrix	304 x 232	192 x 192
Spatial resolution (mm)	1.25 x 1.25	1.98 x 1.98
Temporal resolution (ms)	~30	~20
Slice thickness/gap (mm)	8 mm / 2 mm	8 mm / 2 mm
Flip angle (°)	70	70
Bandwidth (Hz/pixel)	914	898
Heartbeats per slice	14-20	1 or 2*
Cardiac phases	30	18-25*
ECG triggering	Retrospective	Prospective
Breath-holds	10	1 or 2*
Breath-hold duration (s)	10	5-7*

**Heart rate dependent*

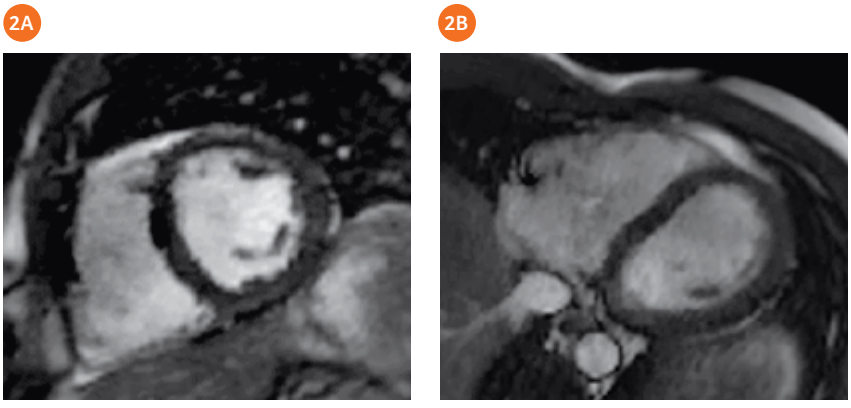

Figure 2. Midventricular LV short-axis and modified RV short-axis images from the highly accelerated CS_bSSFP acquisition (net acceleration 11.5) at end-diastole from the same patient.

2. Short duration of breath-holds to improve patient compliance and to minimize heart rate recovery during suspension of exercise;

3. ECG gating to enable segmented data in discrete cardiac phases for ventricular analysis using commercially available software;

4. Acceptable spatial resolution to delineate ventricular borders for analysis; and

5. Sufficient temporal resolution for accurate determination of end-diastole and end-systole at high heart rates.

To meet all the above requirements, the prototype CS_bSSFP protocol was modified for use under exercise conditions. Typical imaging parameters are given in Table 1. A net acceleration factor of 11.5 was achieved which enables whole heart coverage in one or two breath-holds (5-7 s duration depending on heart rate), with in-plane spatial resolution of 2 mm^2 and temporal resolution in the order of 20 ms. CS_bSSFP images in the LV short-axis (SAX) and modified RV SAX [13] are shown in Figure 2.

Exercise MRI protocol

Pre-MRI exercise testing

Prior to the exercise cardiac MRI, a cardiopulmonary exercise test (CPET) is performed outside the MRI room using a portable metabolic system (Metamax, Cortex BXB, Leipzig, Germany) and an MRI cycle ergometer (Lode, Groningen, The Netherlands). The maximal workload achievable by the patient is determined and then used to calculate the sub-maximal workloads for exercise cardiac MRI. Typically, this is between 25-60 W.

During CPET, the patient is coached by the physiotherapist to hold their breath without valsalva breathing. This is to reduce the potential for intra-thoracic pressure increasing during breath-hold, which in turn could cause reduced venous return and cardiac output.

MRI protocol

After a recovery period, the patient is positioned in the MRI scanner (1.5T, MAGNETOM Aera). ECG and blood oxygen saturation (SPO_2) monitoring is used throughout the examination under the supervision of a cardiologist. After cardiac localizers are obtained, both LV short axis and modified RV short axis stacks are acquired at rest and two pre-determined submaximal workloads (Rest: 0 W, Exercise 1: 25 W and Exercise 2: 40-60 W). In order to achieve steady-state exercise response, subjects cycle at each workload for 3 minutes prior to image acquisition. Between breath-holds, subjects resume cycling for 45 s to return to steady-state exercise response (Fig. 3).

Exercise MRI Analysis

Image analysis is performed off-line using cvi[42] software (Circle Cardiovascular Imaging, Calgary, Canada) and all standard measurements of cardiac function are obtained.

Clinical feasibility

In pilot testing, we demonstrated that this exercise MRI protocol is feasible in patients, healthy controls and in well-trained athletes, with clinically acceptable image quality (Fig. 4). Exercise ergometry within

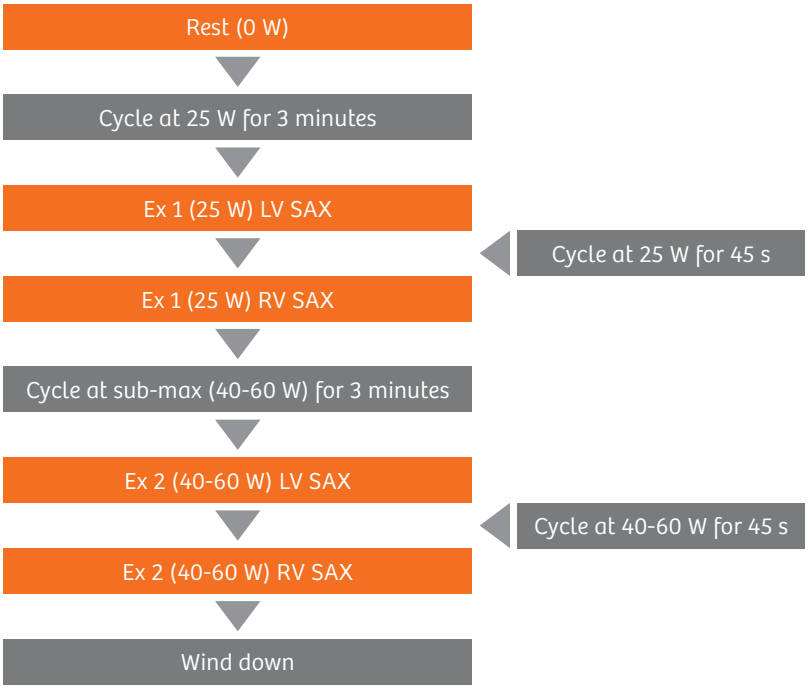

Figure 3. Exercise cardiac MRI study procedure.

the MRI scanner is well tolerated and breath-holds during image acquisition are achievable at submaximal exertion. Quantitative ventricular data and dynamic ventricular response during exercise can be determined using the ultrafast prototype CS_bSSFP sequence.

Clinical applications and potential

Insights from analysis of pressure-volume loops have demonstrated that a ventricle that adapts well is able to increase its contractility to match the chronic increase in afterload and its preservation is important in maintaining ventricular efficiency [14]. Ventricular systolic function adaptation to afterload can be tested dynamically to determine a contractile reserve, the capacity to increase contractility at a given level of loading. Contractile reserve has been shown to be a strong prognostic predictor in patients with left heart failure [15].

Assessment of RV function during exercise may provide an early indication of RV dysfunction and add incremental value in the clinical assessment of patients with right heart disease. In the setting of a chronic pressure overload state such as in pulmonary arterial hypertension (PAH), RV contractile reserve may be a more sensitive marker of hemodynamic ventricular dysfunction.

Currently, there is limited data on RV function during exercise and RV contractile reserve, largely due to the limitations of imaging during exercise. In a small study of pulmonary arterial hypertension (PAH) patients and normal controls, we demonstrated that although having near-normal ventricular function at rest, PAH patients were unable to increase their RV contractile function during exercise [16] (Fig. 5).

Exercise MRI also has the potential to predict adverse surgical outcomes in patients with congenital heart disease undergoing valve replacement surgery. The surgical outcome is likely to be better in patients with a ventricle shown to have contractile reserve. Exercise MRI may enable better-informed decisions about the timing of surgical and therapeutic interventions by detecting early ventricular impairment during exercise (particularly in the right ventricle). By providing information on ventricular contractile reserve, exercise MRI may facilitate improved prognostication of patients and has the potential to predict adverse surgical outcomes.

Conclusions

We have demonstrated that a highly accelerated imaging sequence using compressed sensing can facilitate clinically useful dynamic assessment of biventricular response during exercise with a reliability that was not previously possible.

Acknowledgments

Dr Benjamin Schmitt, Collaboration Manager & Scientific Team Leader MR, Siemens Healthineers ANZ, for technical support with CS sequence.

Dr Richard Slaughter, Radiologist, for clinical advice and expertise.

Mr Andrew Trotter for assistance with MR protocol development and clinical implementation.

Professor Norman Morris and Ms Helen Seale (physiotherapists) for assistance with exercise protocol development and clinical implementation.

The Prince Charles Hospital Foundation for support to purchase the MRI cycle ergometer and ongoing support for the exercise MRI program.

Staff of the Richard Slaughter Centre of Excellence in Cardiovascular MRI for their continued support and dedication.

References

[1] Grothues F, Smith GC, Moon JC, Bellenger NG, Collins P, Klein HU, et al. Comparison of interstudy reproducibility of cardiovascular magnetic resonance with two-dimensional echocardiography in normal subjects and in patients with heart failure or left ventricular hypertrophy. The American journal of cardiology. 2002;90(1):29-34.

[2] Gardner BI, Bingham SE, Allen MR, Blatter DD, Anderson JL. Cardiac magnetic resonance versus transthoracic echocardiography for the assessment of cardiac volumes and regional function after myocardial infarction: an intrasubject comparison using simultaneous intrasubject recordings. Cardiovascular ultrasound. 2009;7:38.

[3] Rayatzadeh H, Patel SJ, Hauser TH, Ngo LL, Shaw JL, Tan A, et al. Volumetric left ventricular ejection fraction is superior to 2-dimensional echocardiography for risk stratification of patients for primary prevention implantable cardioverter-defibrillator implantation. The American journal of cardiology. 2013;111(8):1175-9.

[4] Jiang, L., Handschumacher, M.D., Hibberd, M.G., et al. (1994). Three-dimensional Echocardiographic Reconstruction of Right Ventricular Volume: In Vitro Comparison with Two-dimensional Methods. J. Am. Soc. Echocardiography. 7:150-158.

[5] Pennell, D.J. (2002). Ventricular Volume and Mass by CMR. J. Cardiovasc. Magn. Reson. 4(4):507-513.

[6] Niwa, K., Uchishiba, M., Aotsuka, H., Tobita, K., Matsuo, K., Fujiwara, T., Tateno, S., Hamada, H. (1996). Measurement of Ventricular Volumes by Cine Magnetic Resonance Imaging in Complex Congenital Heart Disease with Morphologically Abnormal Ventricles. Am. Heart Journal. 131(3):567-575.

Figure 4 A-C. Midventricular LV short-axis images at rest and two submaximal workloads at end- diastole using the CS_bSSFP acquisition in a male control.

Figure 4 D-F. Midventricular modified RV short-axis images at rest and two submaximal workloads at end- diastole using the CS_bSSFP acquisition in a female control.

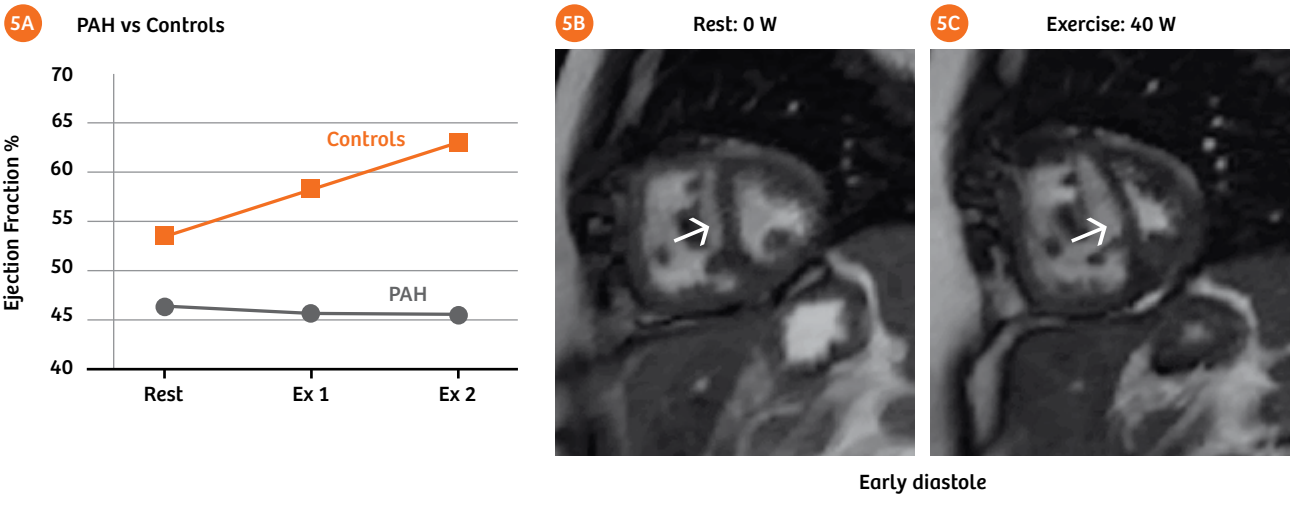

Figure 5A. Exercise MRI unmasks RV dysfunction not evident at rest in patients with pulmonary arterial hypertension (PAH): Despite having near-normal RV function at rest, PAH patients were unable to increase their RV contractile function during exercise.

Figure 5B, C. Midventricular LV short-axis images showing a left-ward deviation of the interventricular septum in early diastole during sub-maximal workload in a pulmonary arterial hypertension patient.

[7]La Gerche A, Claessen G, Van de Bruaene A, et al. Cardiac MRI: a new gold standard for ventricular volume quantification during high-intensity exercise. Circulation. Cardiovascular imaging. Mar 1 2013;6(2): 329-338.

[8]Donoho D. Compressed sensing. IEEE Transactions on Information Theory. 2006;Vol. 52:1289–1306.

[9]Candes E, Romberg J, and Tao T. Robust uncertainty principles: Exact signal reconstruction from highly incomplete frequency information. IEEE Transactions on Information Theory. 2006;Vol. 52:489–509.

[10]Lustig M, Donoho D, Pauly JM. Sparse MRI: The application of compressed sensing for rapid MR imaging. Magnetic resonance in medicine : official journal of the Society of Magnetic Resonance in Medicine / Society of Magnetic Resonance in Medicine. Dec 2007;58(6):1182-1195.

[11]Vincenti G, Monney P, Chaptinel J, Rutz T, Coppo S, Zenge MO, et al. Compressed sensing single-breath-hold CMR for fast quantification of LV function, volumes, and mass. JACC Cardiovascular imaging. 2014;7(9):882-92.

[12]Lin ACW, Strugnell WE, Riley R, Schmitt B, Zeng M, Schmidt M, et al. High Resolution Cine Imaging with Compressed Sensing for Accelerated Clinical Left Ventricular Evaluation. JMRI 2016 (under review/ revision).

[13]Strugnell WE, Slaughter RE, Riley RA, Trotter AJ, Bartlett H. Modified RV short axis series--a new method for cardiac MRI measurement of right ventricular volumes. Journal of cardiovascular magnetic resonance : official journal of the Society for Cardiovascular Magnetic Resonance. 2005;7(5):769-774.

[14]Kuehne T, Yilmaz S, Steendijk P, et al. Magnetic resonance imaging analysis of right ventricular pressure-volume loops: in vivo validation and clinical application in patients with pulmonary hypertension. Circulation. Oct 5 2004;110(14):2010-2016.

[15]Haddad F, Vrtovec B, Ashley EA, Deschamps A, Haddad H, Denault AY. The concept of ventricular reserve in heart failure and pulmonary hypertension: an old metric that brings us one step closer in our quest for prediction. Current opinion in cardiology. Mar 2011;26(2):123-131.

[16]Lin ACW, Strugnell WE, Seale H, Schmitt B, Schmidt M, O'Rouke R, et al. Exercise Cardiac MRI Derived Right Ventriculo-Arterial Coupling Ratio Detects Early Right Ventricular Maladaptation in Pulmonary Arterial Hypertension. ERJ 2016 (in press).

Contact
Ms Wendy Strugnell

Differential Diagnosis of Claudication: Cystic Adventitial Degeneration of the Popliteal Artery—Diagnosis by a Combination of MR Angiography and Anatomical Sequences

Benjamin Henninger, M.D.
Department of Radiology, Medical University of Innsbruck, Innsbruck, Austria

Case Report

A 40-year-old female patient presented at the Department of Vascular Surgery with typical claudication during physical activity after a walking distance of maximum 200 meters. She complained of pain in the right calf that relieved after a short rest. At clinical examination the pulses of the lower extremities were unremarkable at both sides, the oscillogram at rest did not show any pathologies. Under stress the oscillogramm was restricted in the right leg, the treadmill ergometer examination had to be stopped at 3 km/h and 12% fall after 80 meters. The preliminary diagnosis was peripheral artery disease (PAD) grade IIB, a conservative therapy was initially suggested.

The patient was then transferred to our Department of Radiology for the evaluation of PAD. We performed multi-station bolus-chase magnetic resonance angiography (MRA) in the arterial phase of the pelvis and the whole lower extremity (3T, MAGNETOM Skyra, Siemens Healthineers, Erlangen, Germany) in 4 steps using a dedicated peripheral vascular coil together with the body-array and spine-array coils and a fast 3D spoiled gradient echo sequence (T1 3D FLASH) in coronal orientation (TR 3.75 ms, TE 1.33 ms, flip angle: 24°, parallel imaging factor: 3, base resolution: 384, number of slices per slab: 72–80, slice thickness: 1.3 mm, FOV: 420) [1]. A bi-phasic continuous injection of the contrast agent (CA) was used (1 ml/sec and 0.6 ml/sec) together with an automatic movement of the table (table advance per stage: 260–300 mm). Planning of the procedure was done by utilizing the Tim Planning Suite with a Set-n-Go

Figure 1: MR-angiography (3T, MAGNETOM Skyra) clearly depicting an occlusion of the popliteal artery in the P1/P2 segment over a distance of 5 cm with mild collateralization (blue arrows).

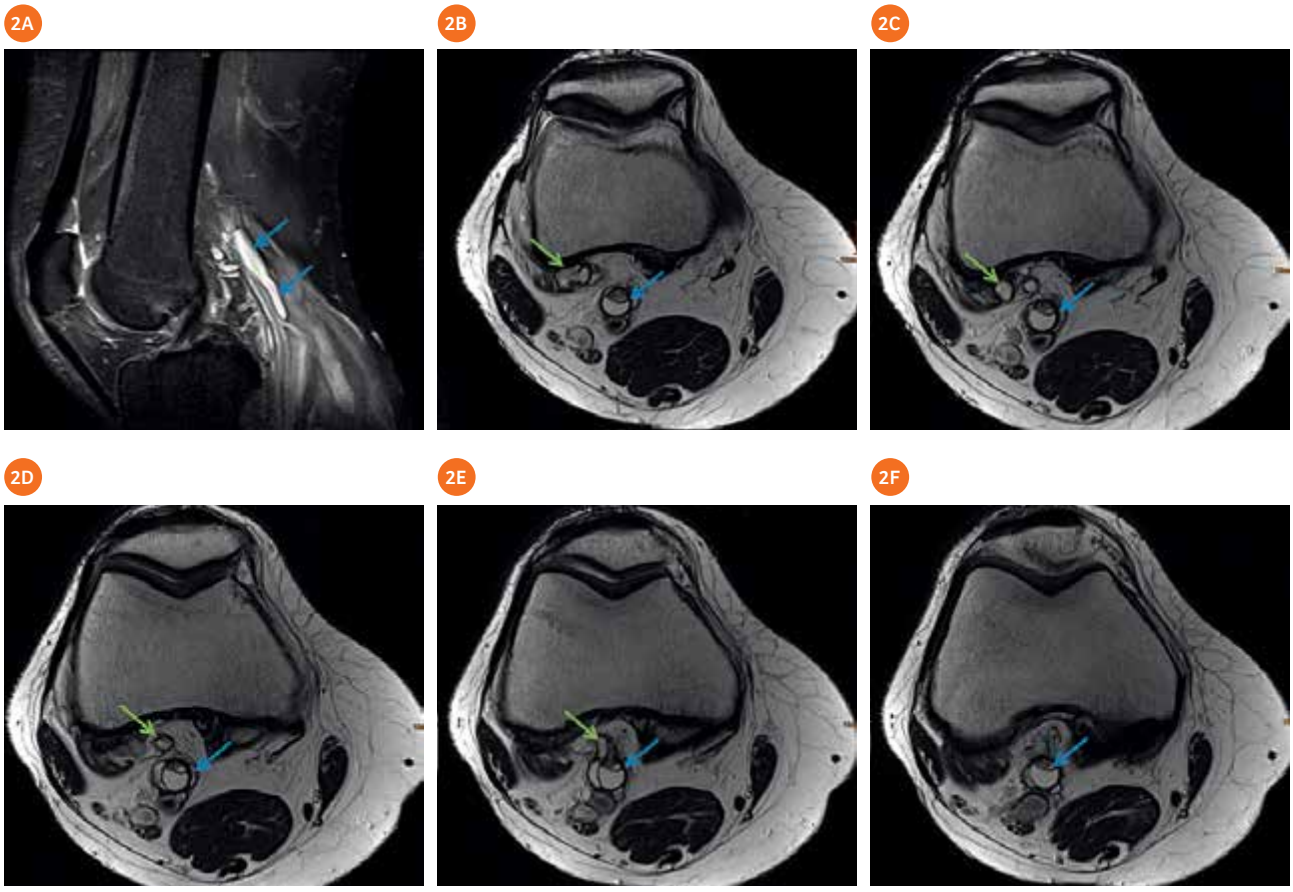

Figure 2: MRI of the knee (1.5T, MAGNETOM Avanto) demonstrating a cystic lesion that is adherent to the popliteal artery (blue arrow). Further we could demonstrate a connection to a ganglion that is adjacent to the knee joint (green arrow). Image **2A** is a sagittal TIRM (TE 15 ms, TR 3160 ms, SL 3 mm, matrix 316 x 320) and images **2C–F** are axial T2-weigthed turbo-spin-echo sequences (TE 79 ms, TR 4680 ms, SL 3 mm, matrix 384 x 384).

protocol. For the timing of the CA the care bolus technique was applied. The MRA showed an occlusion of the popliteal artery in the P1/P2 segment over a distance of 5 cm with mild collateralization (Fig. 1). All the other vessels were unremarkable which is unlikely for a vasosclerotic disease with only one focal manifestation in a young woman. Therefore we decided for a further evaluation by MRI of the knee to rule out other differential diagnosis for the occlusion. We performed knee MRI on a 1.5T scanner (MAGNETOM Avanto, Siemens Healthineers, Erlangen, Germany) with a dedicated knee coil (8-ch high-resolution knee array, Invivo, Gainesville, FL, USA). The protocol consisted of a sagittal TIRM sequence (TE 15 ms, TR 3160 ms, SL 3 mm, matrix 316 x 320) and an axial T2-weigthed turbo-spin-echo sequence (TE 79 ms, TR 4680 ms, SL 3 mm, matrix 384 x 384). We found a cystic lesion (hyperintense on TIRM and T2), adherent to the popliteal artery, with an extraluminal appearance (Fig. 2). The diagnosis was cystic adventitial degeneration of the popliteal artery causing a compression of the artery leading to a stenosis.

The patient was again referred to the Department of Vascular Surgery and due to the clinical burden a surgical procedure was performed. The affected part of the popliteal artery was resected and replaced with the vena basilica by an end to end anastomosis. Postoperative MRA showed a regular opacification of the interponate (Fig. 3). The clinical symptoms disappeared after the intervention and the patient at present is free of any symptoms.

Discussion

The cystic adventitial degeneration is a challenging diagnosis. The disease was initially described by Atkins in 1947 [2]. It is a vascular condition characterized by a collection of mucinous material within the adventitia that constricts the vessel from the outside [3–5]. The P2 segment of the popliteal artery is the most common localization. Patients typically present with the same symptoms as patients with classical PAD. The disease predominantly occurs in young males (age < 50

Figure 3: MR-angiography (3T, MAGNETOM Skyra) after resection of the affected popliteal artery and replacement with the vena basilica by an end-to-end anastomosis. Regular opacification of the interponate is shown (blue arrows).

years) presenting with typical symptoms of claudication. The lack of risk factors for arteriosclerosis and the atypical age should alert for other differential diagnosis. Beside cystic adventitial degeneration other differential diagnosis such as chronic exertional compartment or popliteal entrapment syndrome, chronic venous insufficiency, degenerative disk disease, osteoarthritis, spinal stenosis and thrombangiitis obliterans should also be considered [6].

In some cases MRA can be negative and therefore misleading because the cyst of the adventitia leads to a dynamic exercise-dependent flow inhibition. In our case the occlusion could be clearly depicted with MRI and further associated to a cystic lesion by a local MRI of the knee.

The pathogenesis of cystic adventitial degeneration is still unexplained, but several theories have been advanced:

1. The synovial theory: adventitial cysts are seen as ganglia originating from the adjacent joint space [8].
2. The embryologic theory: inclusion of mucin-secreting cells in the wall of the vessel [8].
3. Microtrauma theory: repeated injuries lead to a progressive degeneration of the arterial adventitia [9, 10].

Our case supports theory 1 because we found a connection between the cyst and ganglia that was adjacent to the knee joint space (Fig. 2).

MRI with a combination of MRA and anatomical sequences are essential tools in the clarification of differential diagnosis in PDA. Further MRI is crucial for surgical planning and also for postoperative control.

References

[1]Nielsen YW, Thomsen HS. Contrast-enhanced peripheral MRA: technique and contrast agents. Acta Radiol. 2012;53(7):769-77.

[2]Atkins HJ, Key JA. A case of myxomatous tumour arising in the adventitia of the left external iliac artery; case report. Br J Surg. 1947;34(136):426.

[3]Rich NM. Popliteal entrapment and adventitial cystic disease. The Surgical clinics of North America. 1982;62(3):449-65.

[4]Korngold EC, Jaff MR. Unusual causes of intermittent claudication: popliteal artery entrapment syndrome, cystic adventitial disease, fibromuscular dysplasia, and endofibrosis. Current treatment options in cardiovascular medicine. 2009;11(2):156-66.

[5]Kiskinis D, Raithel D. Uncommon causes of intermittent claudication: cystic adventitial disease of the popliteal artery and popliteal artery entrapment syndrome. Cardiovascular Research Center bulletin. 1979;17(4):69-74.

[6]Sontheimer DL. Peripheral vascular disease: diagnosis and treatment. American family physician. 2006;73(11):1971-6.

[7]Malghem J, Vande berg BC, Lebon C, Lecouvet FE, Maldague BE. Ganglion cysts of the knee: articular communication revealed by delayed radiography and CT after arthrography. AJR Am J Roentgenol. 1998;170(6):1579-83.

[8]Levien LJ, Benn CA. Adventitial cystic disease: a unifying hypothesis. Journal of vascular surgery. 1998;28(2):193-205.

[9]Chapman T, Pinkerton JA. Cystic adventitial disease of the popliteal artery. Southern medical journal. 1984;77(3):370-2.

[10]Lassonde J, Laurendeau F. Cystic adventitial disease of the popliteal artery. Clinical aspects and etiology. The American surgeon. 1982;48(7):341-3.

Contact
PD Dr. Benjamin Henninger, MD
benjamin.henninger@i-med.ac.at

Quiescent Interval Single-Shot (QISS) Lower Extremity MRA for the Diagnosis of Peripheral Artery Disease: Case Presentations

Akos Varga-Szemes[1]; Thomas M. Todoran[2]; Shivraman Giri[3]; Stephen R. Fuller[1]; U. Joseph Schoepf[1]
[1]Division of Cardiovascular Imaging, Department of Radiology and Radiological Science, Medical University of South Carolina, Charleston, SC, USA
[2]Division of Cardiology, Department of Medicine, Medical University of South Carolina, Charleston, SC, USA
[3]Siemens Healthineers, Chicago, IL, USA

Introduction

Peripheral artery disease (PAD) affects 12%–14% of the general population and its prevalence increases with patient age [1]. While segmental Doppler pressures and pulse volume recording are the most appropriate techniques for screening symptomatic patients, more sophisticated non-invasive imaging techniques may be necessary for further anatomic evaluation and treatment planning, especially before revascularization [2, 3].
The American College of Radiology (ACR) rates both CT angiography (CTA) and MR angiography (MRA) as "usually appropriate" diagnostic approaches for claudication with suspected vascular etiology [2]. Because many patients with PAD suffer from several comorbidities including renal insufficiency, the administration of either iodinated or gadolinium-based contrast media may be of concern given the increased risk of contrast-induced nephropathy or nephrogenic systemic fibrosis (NSF), respectively [4, 5].

These concerns with the risks of contrast media administration in combination with recent technical advances have led to an increased interest in non-contrast MRA techniques. Although many approaches to non-contrast MRA have been evaluated [6], most of them have limited clinical utility in patients with PAD due to either technical issues (e.g. long acquisition time) or overestimation of mild to moderate stenosis [7, 8].

Quiescent-interval single-shot (QISS) MRA is a recently introduced, robust non-contrast MRA technique [9]. QISS MRA at 1.5 and 3T has shown promising results with reported diagnostic accuracies close to or equal to contrast-enhanced MRA [10-14]. Here, we illustrate some of the benefits of QISS MRA over other modalities through two clinical cases and also provide a brief overview of the literature available for this technology.

Discussion

These cases demonstrate certain benefits of QISS MRA over CTA. As emphasized by ACR guidelines, the two major shortcomings limiting image interpretation of CTA in PAD patients are the relatively difficult acquisition timing following contrast administration due to reduced flow in the stenotic vessels and reduced lumen visibility due to heavily calcified atheromatous lesions [2]. As we have shown, QISS MRA is able to overcome both of these limitations to provide reliable findings comparable to invasive DSA.

The QISS MRA technique was first introduced in 2010 by Edelman et al. [9]. This ECG-triggered technique employs initial saturation pulses followed by a 2D single-shot balanced steady-state free precession readout with a quiescent interval between them. Two saturation pulses are used: one to suppress the background signal, and one applied inferior to the slice to suppress the venous blood signal. The quiescent interval before the readout allows the inflow of unsaturated arterial spins into the imaging plane. Due to its design, the flow sensitivity of QISS MRA is negligible compared to other non-contrast techniques such as time-of-flight, 3D fast spin echo based approaches, and ungated ghost MRA [10]. Additionally, single-shot 2D TrueFISP acquisition makes this technique relatively insensitive to patient motion.

Novel technological innovations in development promise to further facilitate the clinical implementation of QISS MRA. QISS MRA can be performed without ECG gating by employing prospective self-navigation based on the detection of the acceleration of blood flow during systole with a reference-less phase contrast navigator [15]. Highly undersampled radial k-space readout

Case 1

A 55-year-old male was referred for evaluation and treatment of intermittent claudication despite adherence to a regular walking program. The patient was a former smoker and his medical history included hyperlipidemia, hypertension, coronary artery disease, PAD, and ANCA-positive vasculitis. Physical examination revealed diminished femoral and popliteal pulses bilaterally. Posterior tibial and dorsalis pedis pulses were Doppler-able. His ankle-brachial index (ABI) was 0.78 in the right leg and 0.91 in the left leg at rest, while ABI severely decreased post exercise (0.53 and 0.52, respectively). In preparation for revascularization the patient was referred for a lower extremity run-off CTA. CTA demonstrated moderate to severe bilateral iliac and superficial femoral artery stenosis. The evaluation of calf vessels was inconclusive as the slower flow in the stenotic vessels delayed the arrival of contrast and thus acquisition occurred before peak enhancement was reached in these vessels. Prior to intervention, the patient underwent a non-contrast QISS MRA on a 1.5T MAGNETOM Avanto scanner. QISS MRA successfully visualized each arterial segment, including those poorly visualized on CTA. In addition to visualizing the stenosis already found on CTA, QISS MRA was able to delineate infrapopliteal run off to the feet. There was total occlusion of the right peroneal artery and total occlusion of the left anterior tibial and posterior tibial arteries. These findings were confirmed by invasive digital subtraction angiography (DSA).

enables the acquisition of multiple 2D slices in a single cardiac cycle shortening the acquisition time of a complete lower extremity runoff MRA to about 2 minutes [16]. High-resolution QISS MRA provides 1.5 mm section thickness and thus more detailed visualization of the vascular anatomy [17]. Quiescent interval low angle shot MRA provides superior image quality for the external carotid arteries compared to 2D time-of-flight with an average acquisition time of less than 6 minutes [18].

The diagnostic accuracy of non-contrast QISS MRA has been evaluated with non-invasive contrast-enhanced MRA as a reference standard, showing a segment-based sensitivity and specificity of 89.7% and 96.5%, respectively [11]. A subgroup analysis in patients who also underwent DSA showed substantial agreement between QISS MRA and DSA [12]. Similarily high sensitivity (98.6%) and specificity (96%) were reported for QISS MRA versus contrast-enhanced MRA in patients with PAD by Klasen et al. [13]. QISS MRA demonstrated superior specificity for detecting hemodynamically significant arterial stenosis in the lower extremities compared to subtracted 3D fast spin echo MRA and was also found to provide higher image quality and diagnostic accuracy in the abdominal and pelvic regions [19].

Case 2

A 65-year-old man was referred for evaluation and treatment of intermittent claudication. Relevant past medical history included hyperlipidemia, hypertension, carotid artery disease, subclavian artery disease, and PAD. Physical examination was remarkable for normal femoral pulses, diminished popliteal pulses and Dopplerable posterior tibial and dorsalis pedis pulses bilaterally. The patient's ABI in the right leg (0.72) was consistent with moderate ischemia, while ABI in the left leg (0.95) was within normal limits at rest. The patient was referred for a lower extremity CTA to plan for revascularization. This demonstrated occluded right superficial femoral, popliteal, anterior tibial, and peroneal arteries and left popliteal, peroneal, anterior tibial, and posterior tibial arteries. Complete lumen visibility was limited due to the presence of heavy calcification, especially in the superficial femoral arteries. As a result, the length of the occlusion could not be determined. Non-contrast QISS MRA (1.5T MAGNETOM Avanto) was performed and was able to sufficiently visualize the entire lower extremity runoff including the heavily calcified segments. QISS MRA provided superior image quality in the calves, visualizing the three vessel runoff in the right calf and the proximal total occlusion of all three left calf vessels filling via collaterals. QISS MRA findings were confirmed with subsequent DSA results.

While the majority of initial QISS MRA studies were performed at 1.5T [9, 11, 12], QISS MRA has also shown good diagnostic accuracy at higher field strength. 3T QISS MRA has high sensitivity (100%) in the presence of adequate image quality for the detection of peripheral artery stenosis when compared to the DSA as a reference standard [14]. Later studies have confirmed the feasibility of QISS MRA at 3T and reported high diagnostic performance and high image quality, especially in the distal segments [20-22].

Conclusion

Past studies have shown that QISS MRA provides high diagnostic accuracy for the detection of hemodynamically significant arterial stenosis of the lower extremities at both 1.5 and 3T. QISS MRA seems to be a feasible alternative for patients in whom contrast media administration is contraindicated, especially in the light of the new ACR guidelines widening the population considered at risk for NSF to patients with eGFR <40 ml/min/1.73m2 [23]. Furthermore, QISS MRA may avoid the timing-related difficulties of contrast-enhanced CTA and better visualize heavily calcified arteries. Finally, its relative insensitivity to blood-flow and patient motion simplifies the patient workflow by requiring minimal user input during the acquisition.

References

[1]Hiatt WR, Hoag S, Hamman RF. Effect of diagnostic criteria on the prevalence of peripheral arterial disease. The San Luis Valley Diabetes Study. Circulation. 1995;91(5):1472-9.

[2]Expert Panel on Vascular Imaging, Dill KE, Rybicki FJ, et al. ACR Appropriateness Criteria® Claudication - Suspected Vascular Etiology. Available at https://acsearch.acr.org/docs/69411/Narrative/. American College of Radiology. Accessed 10/19/2015.

[3]Norgren L, Hiatt WR, Dormandy JA, et al. Inter-society consensus for the management of peripheral arterial disease. Int Angiol. 2007;26(2):81-157.

[4]Davenport MS, Khalatbari S, Cohan RH, Dillman JR, Myles JD, Ellis JH. Contrast material-induced nephrotoxicity and intravenous low-osmolality iodinated contrast material: risk stratification by using estimated glomerular filtration rate. Radiology. 2013;268(3):719-28.

[5]Kuo PH, Kanal E, Abu-Alfa AK, Cowper SE. Gadolinium-based MR contrast agents and nephrogenic systemic fibrosis. Radiology. 2007;242(3):647-9.

[6]Miyazaki M, Lee VS. Nonenhanced MR angiography. Radiology. 2008;248(1):20-43.

[7]Lim RP, Hecht EM, Xu J, et al. 3D nongadolinium-enhanced ECG-gated MRA of the distal lower extremities: preliminary clinical experience. J Magn Reson Imaging. 2008;28(1):181-9.

[8]Haneder S, Attenberger UI, Riffel P, Henzler T, Schoenberg SO, Michaely HJ. Magnetic resonance angiography (MRA) of the calf station at 3.0 T: intraindividual comparison of non-enhanced ECG-gated flow-dependent MRA, continuous table movement MRA and time-resolved MRA. Eur Radiol. 2011;21(7):1452-61.

[9]Edelman RR, Sheehan JJ, Dunkle E, Schindler N, Carr J, Koktzoglou I. Quiescent-interval single-shot unenhanced magnetic resonance angiography of peripheral vascular disease: Technical considerations and clinical feasibility. Magn Reson Med. 2010;63(4):951-8.

[10]Offerman EJ, Hodnett PA, Edelman RR, Koktzoglou I. Nonenhanced methods for lower-extremity MRA: a phantom study examining the effects of stenosis and pathologic flow waveforms at 1.5T. J Magn Reson Imaging. 2011;33(2):401-8.

[11]Hodnett PA, Koktzoglou I, Davarpanah AH, et al. Evaluation of peripheral arterial disease with nonenhanced quiescent-interval single-shot MR angiography. Radiology. 2011;260(1):282-93.

[12]Hodnett PA, Ward EV, Davarpanah AH, et al. Peripheral arterial disease in a symptomatic diabetic population: prospective comparison of rapid unenhanced MR angiography (MRA) with contrast-enhanced MRA. AJR Am J Roentgenol. 2011;197(6):1466-73.

[13]Klasen J, Blondin D, Schmitt P, et al. Nonenhanced ECG-gated quiescent-interval single-shot MRA (QISS-MRA) of the lower extremities: comparison with contrast-enhanced MRA. Clin Radiol. 2012;67(5):441-6.

[14]Hansmann J, Morelli JN, Michaely HJ, et al. Nonenhanced ECG-gated quiescent-interval single shot MRA: Image quality and stenosis assessment at 3 tesla compared with contrast-enhanced MRA and digital subtraction angiography. J Magn Reson Imaging. 2014;39(6):1486-93.

[15]Offerman EJ, Koktzoglou I, Glielmi C, Sen A, Edelman RR. Prospective self-gated nonenhanced magnetic resonance angiography of the peripheral arteries. Magn Reson Med. 2013;69(1):158-62.

[16]Edelman RR, Giri S, Dunkle E, Galizia M, Amin P, Koktzoglou I. Quiescent-inflow single-shot magnetic resonance angiography using a highly undersampled radial k-space trajectory. Magn Reson Med. 2013;70(6):1662-8.

[17]Thierfelder KM, Meimarakis G, Nikolaou K, et al. Non-contrast-enhanced MR angiography at 3 Tesla in patients with advanced peripheral arterial occlusive disease. PLoS One. 2014;9(3):e91078.

[18]Koktzoglou I, Murphy IG, Giri S, Edelman RR. Quiescent interval low angle shot magnetic resonance angiography of the extracranial carotid arteries. Magn Reson Med. 2015.

[19]Ward EV, Galizia MS, Usman A, Popescu AR, Dunkle E, Edelman RR. Comparison of quiescent inflow single-shot and native space for nonenhanced peripheral MR angiography. J Magn Reson Imaging. 2013;38(6):1531-8.

[20]Knobloch G, Gielen M, Lauff MT, et al. ECG-gated quiescent-interval single-shot MR angiography of the lower extremities: initial experience at 3 T. Clin Radiol. 2014;69(5):485-91.

[21]Amin P, Collins JD, Koktzoglou I, et al. Evaluating peripheral arterial disease with unenhanced quiescent-interval single-shot MR angiography at 3 T. AJR Am J Roentgenol. 2014;202(4):886-93.

[22]Wagner M, Knobloch G, Gielen M, et al. Nonenhanced peripheral MR-angiography (MRA) at 3 Tesla: evaluation of quiescent-interval single-shot MRA in patients undergoing digital subtraction angiography. Int J Cardiovasc Imaging. 2015;31(4):841-50.

[23]ACR Committee on Drugs and Contrast Media. ACR Manual on Contrast Media. Version 10.1. 2015.

Contacts

Akos Varga-Szemes, M.D., Ph.D.

Phone +1 843-876-0097

vargaasz@musc.edu

Case Report: QISS MRA at 3T

Anna-Maria Lydon, PgDip MRI, DCR(R)[1]; Associate Professor Andrew Holden, MBChB, FRANZCR[2];
Dr. Jacobus Kritzinger, MBChB, FRCPC[2]
[1]Centre for Advanced MRI, Faculty of Medical & Health Sciences, University of Auckland; New Zealand
[2]Auckland City Hospital, New Zealand

Quiescent Interval Single-Shot (QISS) MR Angiography (MRA) has been shown to be a robust technique for non-contrast MRA of the peripheral vasculature at 1.5T. At 3T, early versions of the sequence offered greater signal-to-noise ratio (SNR) than at 1.5T, but were occasionally compromised by inversion pulse insufficiency due to B_1 nhomogenities. This gave rise to poor venous suppression particularly in the abdominal and pelvic region. We had the opportunity to try a WIP version of the QISS MRA sequence with a modified FOCI pulse which was hoped to overcome aforementioned B_1 inhomogeneities and improve venous suppression whilst maintaining small vessel visualisation on 3T.

We present a case of a 69-year-old male who was referred with short distance left leg claudication, and reduced left femoral pulse, query iliac artery disease. He had a history of smoking 10 cigarettes per day.
The patient was imaged on the 3T MAGNETOM Skyra (Siemens Healthineers, Erlangen, Germany) using the peripheral matrix coil in combination with the spine and body matrix coils. ECG gating was achieved using the Siemens Healthineers wireless PMU.

At the time of imaging the patient had a heart rate of 68 bpm and a recent eGfr of 70 ml/min / 1.73 m^2.

QISS MRA sequences using TrueFISP readout were acquired as a vessel scout technique as this provides an excellent overview for planning subsequent contrast-enhanced (CE) MRA imaging. The standard QISS MRA was used which consists of 1 x 1 x 3 mm contiguous axial slices, single slice per RR interval, flip angle 90°, iPat 3, 40 slices per station. We acquired the abdominal stations during quiet respiration as we found our elderly population cope with this better than with breath-holds and there is no time penalty between techniques.

As per our standard protocol subsequent CE-MRA imaging was performed using diluted 20 ml

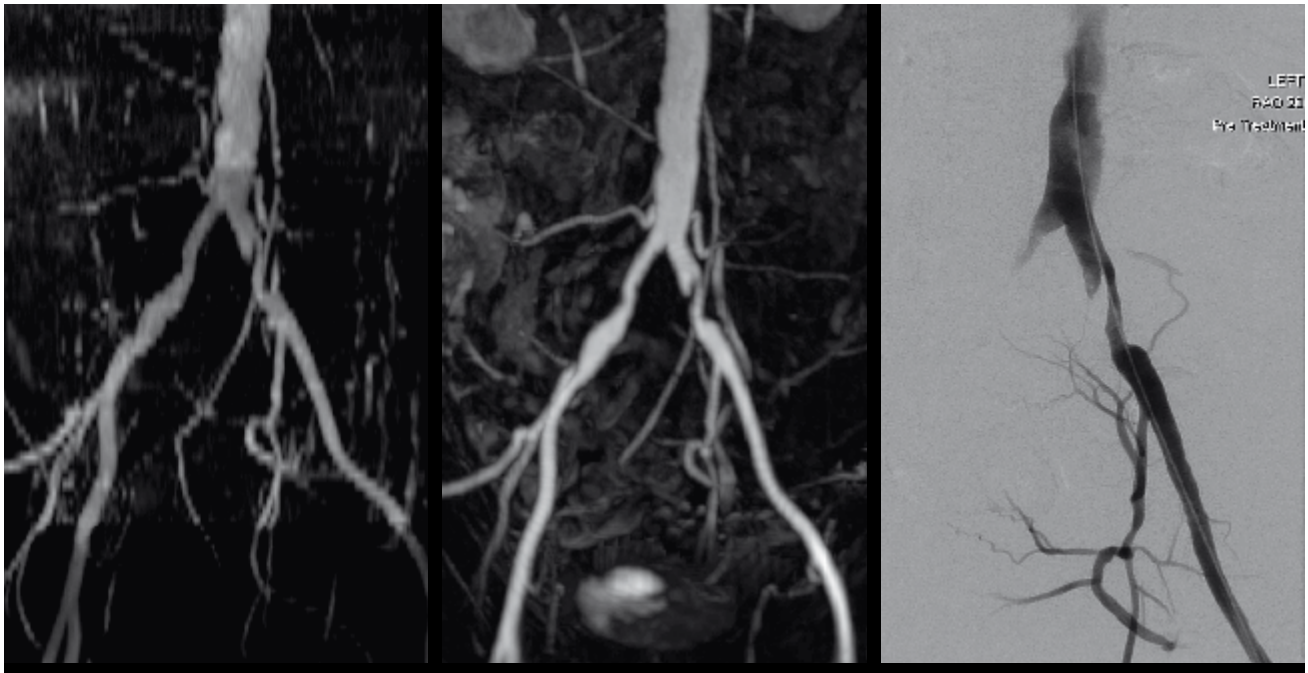

QISS MRA **CE-MRA** **DSA**

Multihance (Gadobenate dimeglumine) + 10 ml 0.9% NaCl, followed by 0.9% NaCl flush. A test bolus of 1.5 ml contrast @ 2 ml/s followed by 20 ml 0.9% NaCl was sampled using a dynamic 2D FLASH single slice positioned at the level of the aortic bifurcation to determine the arrival time of the contrast in the abdominal aorta. Next the tibial arteries were imaged using time-resolved TWIST MRA sequence using 4 ml diluted contrast and a 20 ml NaCl flush delivered @ 2 ml/s. Finally, the full peripheral arterial tree is imaged from above the renal arteries to the pedal arteries using 22-23 ml diluted contrast delivered as follows:

Dual-phase contrast injection:
10 ml @ 2 ml/s, followed by
13 ml @ 1.5 ml/s then an NaCl flush of 20 ml @ 1 ml/s.

Findings included a high-grade stenosis of the mid left common iliac artery. There was also a mild-moderate stenosis of the proximal right common iliac artery. Femoral and popliteal arteries were of normal calibre. There was three vessel run-off to each calf, with severe disease of the left anterior tibial artery and vessel occlusion by mid-calf.

Follow-up DSA confirmed QISS MRA and CE-MRA findings, and the left common iliac artery lesion was treated by angioplasty and stenting with an 8 x 40 mm self-expanding stent, post dilated to 7 mm.

In this case QISS images correlated excellently with the CE-MRA images and subsequent DSA imaging as seen below. We have found that the optimized FOCI pulse is particularly effective in the aorto-iliac region and this case demonstrates very nicely how this new version of the sequence (now product) performs compared to CE-MRA and also DSA.

Acknowledgements

We would like to thank Dr Robert Edelman (Northwestern University, Chicago, IL, USA) and Shivraman Giri (Siemens Healthineers, USA) for providing us with this version of the WIP for evaluation. We would also like to thank Benjamin Schmitt (Siemens Healthineers, Australia) for his support.

Contacts
Anna-Maria Patricia Lydon,
PgDip MRI, DCR(R)
Phone: +64 9 923 9512
a.lydon@auckland.ac.nz

QISS Non-Contrast MR Angiography: A Study of Three Cases with Peripheral Vascular Disease

Maria L. Carr[1]; Shivraman Giri[2]; Sven Zuehlsdorff[2]; Oisin Flanagan[4]; Heron E. Rodriguez[5]; Mark K. Eskandari[5]; Jeremy D. Collins[1]; Robert R. Edelman[3]; James C. Carr[1]
[1]Northwestern University, Department of Radiology, Feinberg School of Medicine, Chicago, IL, USA
[2]Siemens Healthineers, Chicago, IL, USA
[3]Northshore University HealthSystem, Evanston, IL, USA
[4]University of Toronto, Department of Medical Imaging, Ontario, Canada
[5]Northwestern Medicine, Division of Vascular Surgery, Chicago, IL, USA

Introduction

Peripheral arterial disease (PAD) is a common progressive vasculopathy that causes disabling symptoms in the lower extremities, such as diminished arterial pulses, intermittent claudication, rest pain, and can lead to tissue loss. PAD is a common manifestation of the atherosclerotic disease process, affecting from 12% to 14% of the general population [1]. CT angiography (CTA) and contrast-enhanced MR angiography (CEMRA) are the imaging approaches commonly used to evaluate PAD. Many of these patients suffer from renal dysfunction, thus making both CTA and CEMRA less useful due to concerns about contrast-induced nephropathy (CIN) with iodinated contrast or nephrogenic systemic fibrosis (NSF) with gadolinium-based agents [2], respectively. Quiescent-interval single-shot (QISS) imaging employs a stack of 2D TrueFISP images to cover the entire lower extremity and has recently been described as a non-contrast MR angiography technique for assessment of the lower extremity vasculature that demonstrated clinical utility at 1.5T and 3T [3, 4]. In this article we review three cases with QISS MRA demonstrating the clinical utility of this non-contrast technique for supporting physicians in lower extremity arterial evaluation.

Case 1

A 67-year-old male with a history of diabetes mellitus, hypercholesterolemia, and hypertension presented with worsening symptoms of peripheral arterial disease. Five years ago he underwent arterial bypass surgery from the left common femoral artery to the posterior tibial artery with good results. He developed progressively worsening intermittent claudication in the right leg over the last year. His ankle brachial index was 0.62 in the right leg and 1.15 in the left leg. He initially underwent conservative management in a supervised exercise program with limited success. He was then referred for non-invasive imaging with contrast-enhanced MR angiography (CEMRA). His glomerular filtration rate at the time of the CEMRA was greater than 60 cc/min. He underwent a standard 2-injection hybrid CEMRA protocol of the pelvis and lower extremities, which consisted of time resolved TWIST of the calves followed by a timed stepping table, 4-station acquisition of the pelvis and lower extremities on a 3T MAGNETOM Skyra scanner. 0.2 mmol/kg of Gadopentetate dimeglumine was injected intravenously using a divided injection protocol. CEMRA demonstrated a patent left femoral-distal bypass graft and a focal stenosis in the right superficial femoral artery. There was significant venous contamination of the calf vessels bilaterally, more severe on the right, which precluded accurate assessment of the runoff vessels. A QISS non-contrast MRA exam, performed at the same imaging session just before the contrast injection, also showed a patent left femoral-distal bypass graft and a focal stenosis in the right superficial femoral artery.

1B

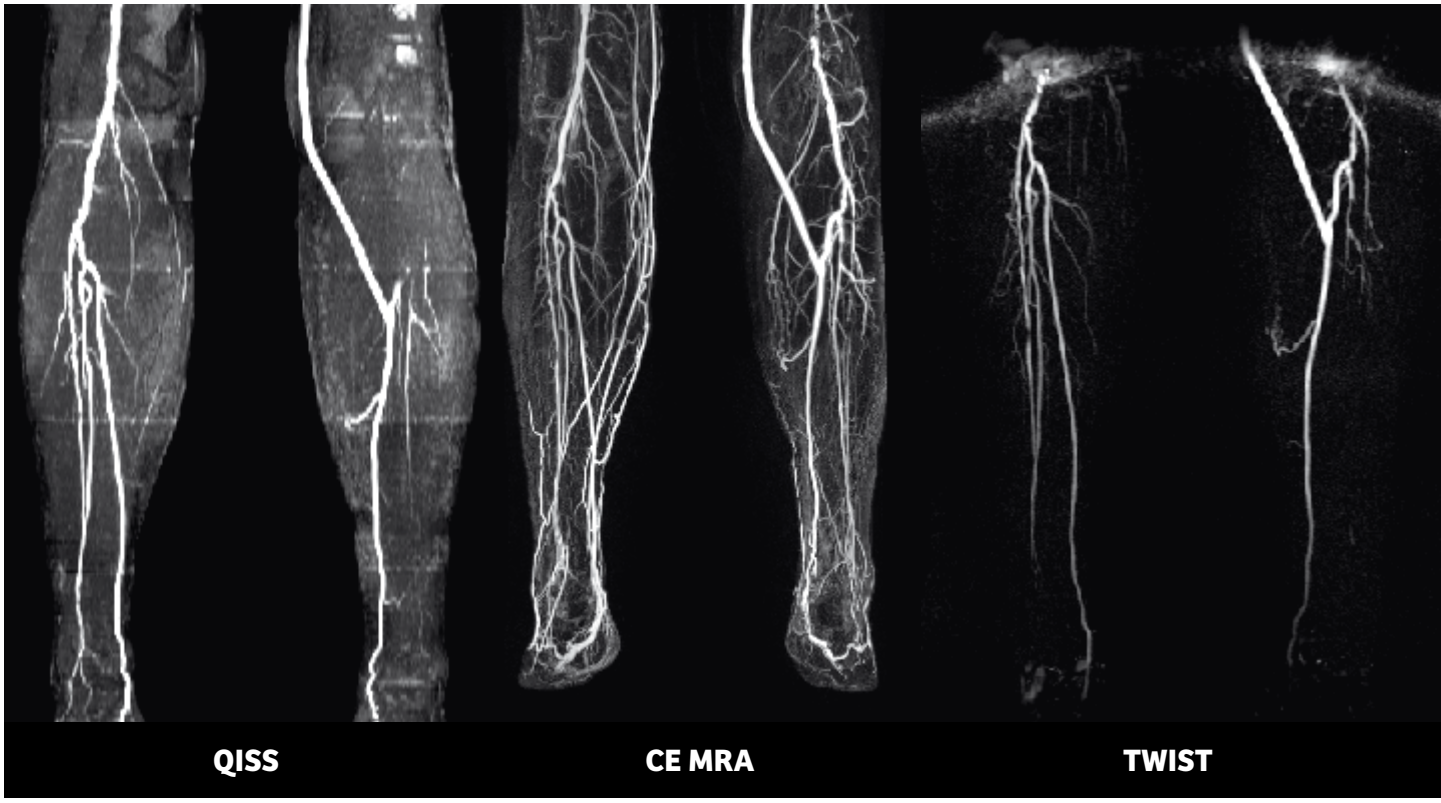

Case 2

A 79-year-old male with hypertension, prostate cancer, and ischemic cardiomyopathy status post coronary artery bypass surgery, presented with worsening bilateral intermittent calf claudication. He was unable to walk one block without pain. He initially underwent non-invasive vascular testing; however ankle brachial indices were found to be invalid due to extensive calcification in the runoff vessels. He then underwent CT angiography, which showed extensive calcification of his peripheral vasculature, notably of the calves, which limited assessment of stenosis severity of the infrapopliteal vessels. The patient was referred for contrast-enhanced MRA, which confirmed CT findings with diffuse mild disease in the inflow and outflow segments and demonstrated bilateral moderate to severe tibial artery disease. Assessment of the left tibial vessels was limited by venous contamination, precluding evaluation of the distal anterior tibial and posterior tibial arteries. QISS MRA was performed or further assessment of the tibial vasculature, confirming patency of the bilateral posterior tibial and peroneal arteries, with occlusion of the anterior tibial arteries. There was perfect agreement between QISS MRA and CEMRA in the right calf, and QISS MRA was diagnostic in the left calf, demonstrating similar findings compared to CT angiography without the limitation of artifact from diffuse vascular calcificaitons. In particular, the left plantar arteries are patient on QISS MRA while the dorsalis pedis is seen to be occluded. Of note, the symmetric loss of signal noted in the pelvis and proximal thighs on QISS MRA is typical for 'striping' artifacts from intermittent ectopy resulting in misgating. The symmetry of this appearance reassures the reader that this represents artifact rather than real disease. If poor gating limits evaluation of a particular station, the station can be reacquired in just 45 seconds without the need to re-shim.

2

Case 3

An 86-year-old male with a history of cancer, hypertension and diabetes presented with left leg claudication. The patient had a history of renal dysfunction with eGFR < 30 ml/min/1.73 m², so contrast-enhanced MRA was not an option. The referring physician therefore ordered a non-contrast MRA. The QISS images showed a long left-sided superficial femoral artery occlusion with single-vessel runoff to the foot via the posterior tibial artery. On-table angiography in the operating room, using minimal amounts of contrast, confirmed the vascular findings and a bypass graft was placed. Therefore, this patient with severe renal dysfunction was diagnosed and treated without the need for a gadolinium-based contrast agent and minimal iodinated contrast.

3

Discussion

In this report, we described three cases that illustrate the potential utility of non-contrast MR angiography using QISS in the clinical setting. QISS MRA is a simple to use technique that provides excellent image quality with high diagnostic yield in relatively short acquisition times. Besides, QISS MRA can be an alternative to CEMRA, thereby resulting in significant cost savings by avoiding costs associated with gadolinium contrast administration and point of care eGFR testing. QISS protocol can be run in about half the time of a standard CEMRA runoff protocol leading to improved patient throughput. Since QISS is largely automated and image processing occurs inline, technologists can be attending to other tasks while scanning is taking place, leading to greater staff efficiency.

Traditionally, non-contrast MR angiography of the lower extremities relied on an ECG-gated 2D time of flight approach. However, this approach has the disadvantage of very long acquisition times and variable image quality, particularly in regions of disease and vessel tortuosity [5]. Newer approaches have focused on subtractive methods, using either fast spin echo [6] or balanced steady state free precession readouts [7]. These techniques depend on the variation in blood signal between systole and diastole. Both arteries and veins appear bright in diastole, whereas only veins are visible in systole. Therefore, a subtracted dataset can produce a pure arterial image. Unfortunately, this imaging technique can be unreliable and its complexity, e.g. the requirement to subtract two image sets and necessary patient specific adjustments reduces clinical utility and makes it challenging to use for technologists who do not have extensive experience with it.

The QISS technique acquires stacks of axial slices to cover the region of interest, which in the case of the peripheral vasculature is from pelvis to feet. Each image stack is acquired near the magnet isocenter in order to avoid artifacts from off-resonance effects. Each stack automatically undergoes inline maximum intensity projection (MIP) processing. Auto compose assembles these together at the end of the acquisition to produce a MIP of the entire peripheral vasculature. A key advantage of QISS is the simplicity of the acquisition technique and protocol set up, reducing dependence on experienced MR technologists. ECG leads are applied at the beginning of the test and the patient is placed supine, feet first with a peripheral vascular coil as with the usual runoff protocol. Since it is an axial acquisition, there is no time spent with setting up slices orientations and there is no risk to excluding regions of the vascular anatomy, as can occur with oblique coronal acquisitions tailored to the vascular anatomy to optimize the imaging time. The acquisition time is typically 8-10 minutes depending on heart rate. The images are acquired without operator intervention enabling the technologist to perform other tasks while scanning is taking place, and improving work efficiency. Moreover, since most of the image processing occurs inline, there is no need for advanced image analysis using other software algorithms or specialized post-processing staff.

Initial experience at 3T revealed two sporadic image quality issues in pelvic and abdominal stations: (1) Undesirable venous signal and (2) insufficient arterial conspicuity. These are possibly related to B_1-field inhomogeneity issues typically seen at higher field strengths.

QISS MR angiography has been extensively validated in the medical literature, both at 1.5T and 3T. The initial paper by Hodnett et al. [8], which evaluated 53 patients at 1.5T in a two-center trial using both contrast-enhanced MRA and digital subtraction angiography as reference standards, found high sensitivities and specificities for QISS when compared to both CEMRA and DSA. In fact, QISS performed slightly better that CEMRA when compared to DSA in a patient subgroup and, also in this study, QISS performed well irrespective of renal function. In a second study of 25 patients with diabetes mellitus, QISS compared well to both CEMRA and DSA for detection of significant disease [4]. In another study comparing QISS to a non-contrast, ECG-gated 3D single shot fast spin echo pulse sequence in 20 patients, QISS demonstrated superior specificity and image quality, and was more robust in the abdominal and pelvic regions [9]. QISS MRA has also been extensively studied at 3T and results are similar to 1.5T showing high diagnostic accuracy and excellent image quality [10]. Recent technical advances promise to overcome limitations of B_1 field inhomogeneity and high power deposition, thereby further improving the performance at 3T.

Each of our cases demonstrates some of the advantages of QISS MRA.

Case 1 is of a diabetic patient who had previously undergone a left leg bypass graft. Stepping table contrast-enhanced MR angiography using a four-station approach on a 3T MAGNETOM Skyra resulted in venous contamination in the calf vessels due to suboptimal timing of contrast agent injection, precluding accurate evaluation. Early venous enhancement in this case was likely due to fast transit down the left leg due to the bypass graft and soft tissue inflammation in the right leg. Venous contamination is known to occur in up to 20% of cases using a single injection, stepping table CEMRA protocol. Several attempts to solve this problem for CEMRA include using a 2-injection protocol, where the calves are imaged first, or else attaching blood pressure cuffs on the thighs to slow venous return. Both approaches lengthen and complicate the protocol. Another solution is to use QISS as an alternative or adjunct to CEMRA. In our case, the QISS images clearly show the left sided bypass graft and the calf vessels without any overlap of adjacent veins.

In case 2, non-invasive vascular testing was non-diagnostic due to heavily calcified vessels, which also impaired diagnosis by CT angiography. Most of the disease was confined to the infra-popliteal segments. QISS was comparable to CEMRA for depiction of the runoff vessels and both were superior to CTA.

In case 3, a patient with diabetes presented with left leg claudication but had renal dysfunction with an eGFR of 50 ml/min. The referring physician did not want to use either a MR or CT contrast agent, so that QISS MR angiography provided a helpful diagnostic solution. The QISS images showed a long left-sided superficial femoral artery occlusion with single vessel runoff to the foot, which was sufficient information for the vascular surgeon to plan arterial bypass.

In conclusion, QISS MR angiography is a robust, simple and reliable non-contrast technique that can be used

at 1.5T and 3T. QISS MRA has been extensively evaluated in several studies, including diabetic patients in whom renal dysfunction and vascular calcifications are particularly common and infra-popliteal disease is usually more severe. QISS MRA should become the non-contrast MRA technique of choice in patients with renal dysfunction. It may be particularly suitable for diabetic patients or those already on dialysis where vascular calcification is particularly prevalent. Although QISS MRA is robust with an imaging protocol that can be run without patient-specific modifications, patients with frequent ectopy or irregular arrhythmias demonstrate symmetric mis-gating artifacts (Fig. 2) which can reduce image quality of QISS MRA. QISS MRA can also be employed as an alternative to CEMRA resulting in potential cost savings by avoiding the costs of the contrast agent and associated infusion paraphernalia, as well as by improving patient throughput.

The statements by Siemens Healthineers customers described herein are based on results that were achieved in the customer's unique setting. Because there is no "typical" hospital or laboratory and many variables exist (e.g., hospital size, samples mix, case mix, level of IT and/or automation adoption) there can be no guarantee that other customers will achieve the same results.

References

[1]Hiatt WR, Hoag S, Hamman RF. Effect of diagnostic criteria on the prevalence of peripheral arterial disease. The San Luis Valley Diabetes Study. Circulation 1995;91:1472-9.

[2]Sadowski EA, Bennett LK, Chan MR, et al. Nephrogenic systemic fibrosis: risk factors and incidence estimation. Radiology 2007;243:148-57.

[3]Edelman RR, Sheehan JJ, Dunkle E, Schindler N, Carr J, Koktzoglou I. Quiescent-interval single-shot unenhanced magnetic resonance angiography of peripheral vascular disease: Technical considerations and clinical feasibility. Magnetic resonance in medicine : official journal of the Society of Magnetic Resonance in Medicine / Society of Magnetic Resonance in Medicine 2010;63:951-8.

[4]Hodnett PA, Ward EV, Davarpanah AH, et al. Peripheral arterial disease in a symptomatic diabetic population: prospective comparison of rapid unenhanced MR angiography (MRA) with contrast-enhanced MRA. AJR American journal of roentgenology 2011;197:1466-73.

[5]Offerman EJ, Hodnett PA, Edelman RR, Koktzoglou I. Nonenhanced methods for lower-extremity MRA: a phantom study examining the effects of stenosis and pathologic flow waveforms at 1.5T. Journal of magnetic resonance imaging : JMRI 2011;33:401-8.

[6]Lanzman RS, Blondin D, Schmitt P, et al. Non-enhanced 3D MR angiography of the lower extremity using ECG-gated TSE imaging with non-selective refocusing pulses--initial experience. RoFo : Fortschritte auf dem Gebiete der Rontgenstrahlen und der Nuklearmedizin 2010;182:861-7.

[7]Lanzman RS, Schmitt P, Kropil P, Blondin D. [Nonenhanced MR angiography techniques]. RoFo : Fortschritte auf dem Gebiete der Rontgenstrahlen und der Nuklearmedizin 2011;183:913-24.

[8]Hodnett PA, Koktzoglou I, Davarpanah AH, et al. Evaluation of peripheral arterial disease with nonenhanced quiescent-interval single-shot MR angiography. Radiology 2011;260:282-93.

[9]Ward EV, Galizia MS, Usman A, Popescu AR, Dunkle E, Edelman RR. Comparison of quiescent inflow single-shot and native space for nonenhanced peripheral MR angiography. Journal of magnetic resonance imaging : JMRI 2013;38:1531-8.

[10]Knobloch G, Gielen M, Lauff MT, et al. ECG-gated quiescent-interval single-shot MR angiography of the lower extremities: initial experience at 3 T. Clinical radiology 2014;69:485-91.

Contacts
Maria L. Carr, RT.R (CT)(MR)
MRI Corporate Supervisor
NorthShore University HealthSystem
Walgreen Building, Suite G507
2650 Ridge Avenue
Evanston, IL 60201
USA
Phone: +1 847-570-4349
MCarr@northshore.org

Pictorial Essay: Pulmonary Imaging for Children

Sonja Kinner, M.D.; Haemi Phaedra Schemuth, M.D.
Department of Diagnostic and Interventional Radiology, University Hospital Essen, Essen, Germany

Introduction

To detect pulmonary metastasis a computed tomography (CT) scan is still the gold standard for adults as well as children. However, for children we try to keep the radiation burden as low as possible and use magnetic resonance imaging (MRI) for as many examinations as possible*. Especially in children with oncologic diseases that can be treated curatively, we use MRI for the cervical and abdominal staging examinations and often also use the MRI for the thoracic staging of the axillary, hilar, and mediastinal lymph nodes. However, to assess pulmonary metastases it is still necessary to perform a chest CT scan.

**MR scanning has not been established as safe for imaging fetuses and infants under two years of age. The responsible physician must evaluate the benefit of the MRI examination in comparison to other imaging procedures.*

The examination we usually use for a thoracic MRI for children typically consists of a short TI inversion recovery (STIR) sequence, a T2-weighted half fourier single-shot turbo spin echo (HASTE) sequence, a T1-weighted turbo spin echo (TSE) sequence, a true fast imaging with steady-state free precession (TrueFISP) sequence, dynamic volume interpolated breath-hold examination (VIBE) sequences, and a T1-weighted fast low angle shot (FLASH) 2D sequence. However in all of these sequences we have quite a few, especially motion artifacts and can only safely assess pulmonary metastases when they have a diameter of at least 10 mm. For the staging in oncologic patients it is though also important to assess small pulmonary nodules, therefore we still rely on CT scans.

With FREEZEit, which includes the free-breathing radial MRI sequence StarVIBE we have less motion artifacts and may be able to assess pulmonary metastases.

Reference

H Chandarana, KT Block, MJ Winfeld, SV Lala, D Mazori, E Giuffrida, JS Babb, SS Milla. Free-breathing contrast-enhanced T1-weighted gradient-echo imaging with radial k-space sampling for paediatric abdominopelvic MRI. Eur Radiol (2014) 24:320-326.

Contact
Priv.-Doz. Dr. med. Sonja Kinner
Sonja.Kinner@uni-due.de

Case 1

5-year-old male patient with an anaplastic large T-cell lymphoma with cervical and axillary lymphomas. For staging purposes a contrast-enhanced MRI of the abdomen and neck was performed as well as a contrast-enhanced CT and MRI scan of the chest. The cervical MRI scan showed cervical and axillary lymphomas; the CT and MRI scan of the chest showed left hilar lymphadenopathy with a consecutive dystelectasis of the left upper lobe.

1 Contrast-enhanced CT scan in an arterial phase in **(1A)** lung window and **(1B)** ediastinal window (SOMATOM Definition Flash; 3 mm slice thickness) show mediastinal lymphoma and dystelectasis of the left upper lobe. **(1C)** The StarVIBE sequence (MAGNETOM Aera 1.5T; 3 mm slice thickness) displays the mediastinal and axillary (arrow) lymph nodes in the post-contrast phase at least as well as in the CT scan.

Case 2

3-year-old male patient with post-transplant lymphoproliferative disorder (PTLD) after kidney transplantation.

The patient initially presented as a premature baby with a renal vein thrombosis. This led to a consecutive kidney failure and kidney transplant. Four months after the kidney transplant the patient developed a PTLD with cervical, mediastinal, mesenteric, retroperitoneal, pelvic and pulmonal lymphomas. An FDG-PET/CT scan without an intravenous contrast agent was performed as well as an MRI of the chest and abdomen.

2A

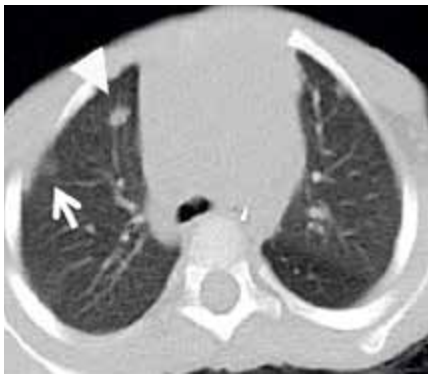

2B

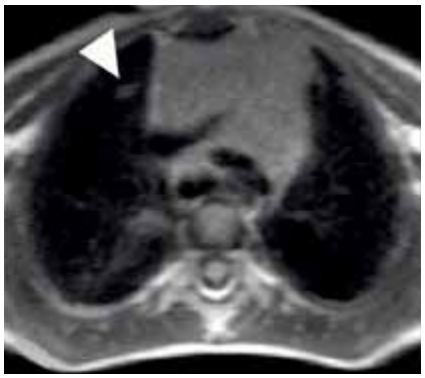

2C

2 **(2A)** The non-contrast CT scan (3 mm slice thickness) in lung window shows pulmonary and mediastinal lymphoma manifestations. **(2B)** In a T2-weighted HASTE sequence (MAGNETOM Aera 1.5T; 5 mm slice thickness) only the bigger pulmonary lesion can be detected (arrowhead), while **(2C)** StarVIBE (MAGNETOM Aera 1.5T; 3 mm slice thickness) is able to show additional lung lesions (arrow).

Case 3

9-year-old male patient with a peripheral t-cell lymphoma.

The patient presented with cervical, thoracic, and abdominal lymphomas. Staging was done by a ^{18}F-FDG-PET/CT without intravenous contrast agent and a contrast-enhanced cervical, thoracic, and abdominal MRI.

3A

3B

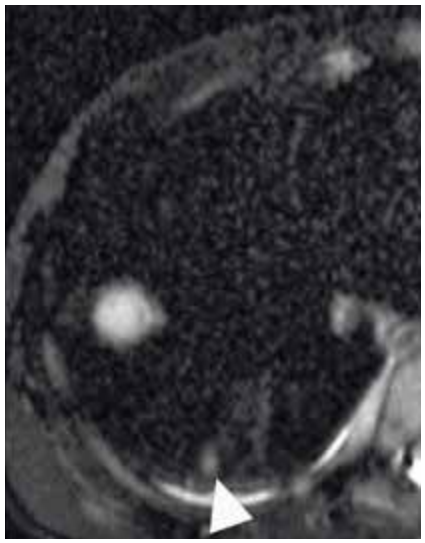

3C

3 **(3A)** Non-contrast CT scan in lung window (3 mm slice thickness) shows two pulmonary lymphoma manifestations, which are also shown by **(3B)** the T2-weighted HASTE sequence however with less spatial resolution than **(3C)** the StarVIBE. In the StarVIBE sequence the second pulmonary lymphoma manifestation is masked by a dystelectasis (arrow). In our protocol, StarVIBE is the last sequence, which can lead to dystelectasis, especially after a quite extensive imaging protocol for whole-body staging. Therefore, it would be advisable to perform this sequence as early as possible.

Case 4

14-year-old female patient with acute lymphatic leukemia (ALL) and aspergillosis.

Patient presented with invasive aspergillosis after receiving chemotherapy with aspergillosis manifestations in the lungs as well as the liver.

4A

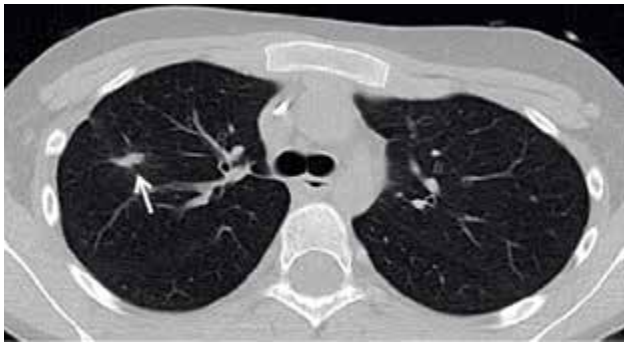

4B

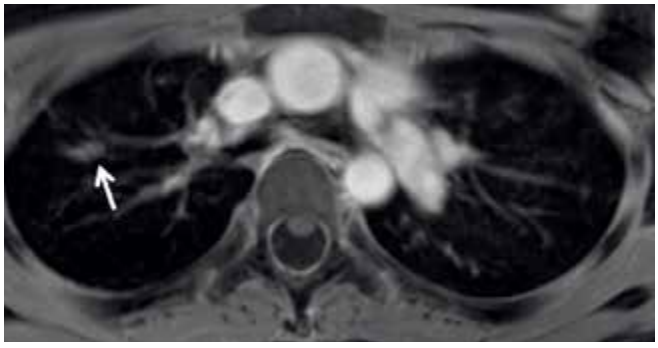

4 Single aspergillosis lesion in the upper right lobe in **(4A)** the non-contrast CT scan, with the same lesion shown in **(4B)** the StarVIBE sequence.

Case 5

2-year-old male patient with PTLD.

Patient presented with liver cirrhosis, and hepatocellular carcinoma (HCC). He received a liver transplant, and shortly after developed PTLD. An FDG-PET/CT was performed, as well as a cervical, thoracic, and abdominal MRI. Pulmonary lymphomas were not detected, however infiltrates were diagnosed.

5A

5B

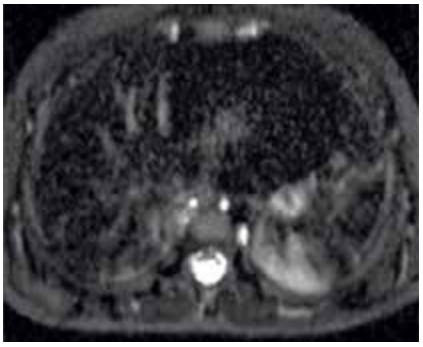

5C

5 **(5A)** The CT scan and **(5C)** the StarVIBE sequence show the infiltrates in both lower lobes. **(5B)** The T2-weighted HASTEsequence does not offer as much spatial resolution as the CT scan and the StarVIBE.

At Siemens Healthineers, our purpose is to enable healthcare providers to increase value by empowering them on their journey towards expanding precision medicine, transforming care delivery, and improving patient experience, all enabled by digitalizing healthcare.

An estimated 5 million patients globally everyday benefit from our innovative technologies and services in the areas of diagnostic and therapeutic imaging, laboratory diagnostics and molecular medicine, as well as digital health and enterprise services.

We are a leading medical technology company with over 170 years of experience and 18,000 patents globally. With more than 48,000 dedicated colleagues in 75 countries, we will continue to innovate and shape the future of healthcare.

On account of certain regional limitations of sales rights and service availability, we cannot guarantee that all products included in this brochure are available through the Siemens Healthineers sales organization worldwide.

Availability and packaging may vary by country and is subject to change without prior notice. Some/All of the features and products described herein may not be available in the United States.

The information in this document contains general technical descriptions of specifications and options as well as standard and optional features, which do not always have to be present in individual cases.

Siemens Healthineers reserves the right to modify the design, packaging, specifications, and options described herein without prior notice. For the most current information, please contact your local sales representative from Siemens Healthineers.

Note: Any technical data contained in this document may vary within defined tolerances. Original images always lose a certain amount of detail when reproduced.

The outcomes and statements provided by customers of Siemens Healthineers are unique to each customer's setting. Since there is no "typical" hospital and many variables exist (e.g., hospital size, case mix, and level of service/technology adoption), there can be no guarantee that others will achieve the same results.

Siemens Healthineers Headquarters
Siemens Healthcare GmbH
Henkestr. 127
91052 Erlangen, Germany
Phone: +49 9131 84-0
siemens-healthineers.com

Local Contact Information
Siemens Medical Solutions USA, Inc.
40 Liberty Boulevard
Malvern, PA 19355-9998, USA
Phone: 1-888-826-9702
siemens-healthineers.us

Order No. 20-18-10707-01-76 · Online Pdf · 05-2018 ·